Signal transmission within the P2X$_2$ trimeric receptor

Batu Keceli[1] and Yoshihiro Kubo[1,2]

[1]Division of Biophysics and Neurobiology, Department of Molecular Physiology, National Institute for Physiological Sciences, Aichi 444-8585, Japan

[2]Department of Physiological Sciences, The Graduate University for Advanced Studies, School of Life Science, Kanagawa 240-0155, Japan

P2X$_2$ receptor channel, a homotrimer activated by the binding of extracellular adenosine triphosphate (ATP) to three intersubunit ATP-binding sites (each located ∼50 Å from the ion permeation pore), also shows voltage-dependent activation upon hyperpolarization. Here, we used tandem trimeric constructs (TTCs) harboring critical mutations at the ATP-binding, linker, and pore regions to investigate how the ATP activation signal is transmitted within the trimer and how signals generated by ATP and hyperpolarization converge. Analysis of voltage- and [ATP]-dependent gating in these TTCs showed that: (a) Voltage- and [ATP]-dependent gating of P2X$_2$ requires binding of at least two ATP molecules. (b) D315A mutation in the β-*14* strand of the linker region connecting the ATP-binding domains to the pore-forming helices induces two different gating modes; this requires the presence of the D315A mutation in at least two subunits. (c) The T339S mutation in the pore domains of all three subunits abolishes the voltage dependence of P2X$_2$ gating in saturating [ATP], making P2X$_2$ equally active at all membrane potentials. Increasing the number of T339S mutations in the TTC results in gradual changes in the voltage dependence of gating from that of the wild-type channel, suggesting equal and independent contributions of the subunits at the pore level. (d) Voltage- and [ATP]-dependent gating in TTCs differs depending on the location of one D315A relative to one K308A that blocks the ATP binding and downstream signal transmission. (e) Voltage- and [ATP]-dependent gating does not depend on where one T339S is located relative to K308A (or D315A). Our results suggest that each intersubunit ATP-binding signal is directly transmitted on the same subunit to the level of D315 via the domain that contributes K308 to the β-*14* strand. The signal subsequently spreads equally to all three subunits at the level of the pore, resulting in symmetric and independent contributions of the three subunits to pore opening.

INTRODUCTION

P2X receptors are extracellular ATP-gated nonselective cation channels (Valera et al., 1994; North, 2002), which are widely expressed in many physiological systems and play various important functional roles (Khakh, 2001; Khakh et al., 2001; North, 2002; Inoue et al., 2005; Burnstock, 2007a,b, 2008). P2X receptors are trimers with identical or related subunits and are structurally quite distinct from other ligand-gated channels such as glutamate and cys-loop receptors (Khakh, 2001; Khakh et al., 2001; North, 2002; Inoue et al., 2005; Burnstock, 2007a,b, 2008).

Recent crystal structure data of P2X$_4$ from zebra fish revealed that each P2X subunit has two transmembrane (TM) helices (TM1 and TM2) and a large extracellular domain (Kawate et al., 2009). The pore is formed by three TM2 helices from each subunit, which are steeply angled to the membrane (Kawate et al., 2009; Hattori and Gouaux, 2012), and those pore-forming three TM2 helices are surrounded by three TM1 helices that are assumed to be necessary to hold the pore in the closed

state and do not directly contribute to ion flow (Kawate et al., 2009; Li et al., 2010; Hattori and Gouaux, 2012). Extracellular ATP activates the trimeric structure by binding to the three intersubunit-binding sites, which leads to conformational rearrangements that are transferred to pore-forming TM helices linked to ATP-binding domains by β strands (Fig. 1; Kawate et al., 2009; Hattori and Gouaux, 2012).

We showed previously that P2X$_2$ receptor activation is not only dependent on ligand binding but also on the membrane potential, in spite of the absence of a canonical voltage sensor (Fujiwara et al., 2009; Keceli and Kubo, 2009; Kubo et al., 2009). The P2X$_2$ receptor shows a gradual single-exponential activation upon hyperpolarizing step pulses in the steady state after application of ATP (Fujiwara et al., 2009). The speed of activation accelerates with the increase in the [ATP]. Furthermore, the tail current analysis at various [ATP] reveals a concentration-dependent G-V shift to depolarized potentials (Fujiwara et al., 2009). Those results

Correspondence to Batu Keceli: bkeceli@nips.ac.jp

Abbreviations used in this paper: TM, transmembrane; TTC, tandem trimer construct.

indicate that gating of the P2X receptor is dependent not only on ATP activation but also on membrane potential. Voltage sensitivity of the P2X$_2$ receptor channel is an intrinsic property. The channel is devoid of any secondary mechanisms such as voltage-dependent block/ unblock by some positively charged cations or substances, or an inactivation "ball" mechanism observed in *Shaker* K$^+$ channels (Zhou and Hume, 1998; Fujiwara et al., 2009; Kubo et al., 2009).

For ligand-gated channels, the pore is a region that allows permeation of ions. It is not yet fully clarified for P2X receptors how the trimeric structure rearranges itself from closed to open by ligand binding–induced perturbations, which take place ∼50 Å away from the pore. Moreover, how the activation signal propagates down to the pore, how subunits couple to each other in the conformational rearrangement, and the exact number of bound ATP molecules required for full activation by voltage- and [ATP]-dependent gating remain unknown.

Our ultimate aim in this study is to clarify especially from the aspect of stoichiometry, how the activation signal propagates in the P2X$_2$ trimer from the ATP binding to the pore opening, and how signals generated by ATP binding and hyperpolarization converge. Toward these aims, we introduced mutations at the ATP-binding site (K308A), the pore region (T339S), and the linker region between them (D315A). The characteristic feature of these mutations is that each of them creates radical changes in the voltage- and [ATP]-dependent gating of the P2X$_2$ receptor when inserted into all three subunits. We prepared tandem trimer constructs (TTCs) by insertion of critical mutations at one, two, or three subunits at one time to determine how many subunits the activation signal propagates through at different levels from the ATP-binding sites to the pore level (Fig. 1). Furthermore, to track the activation signal from the ATP-binding site to the pore level, i.e., whether the signal travels on the ATP-bound subunit or spreads to other subunits, we made various combinations of these mutants in tandem repeat constructs and analyzed voltage- and [ATP]-dependent gating.

MATERIALS AND METHODS

In vitro mutagenesis and cRNA synthesis
A BamH1-Not 1 fragment of the original rat P2X$_2$ cDNA (provided by D. Julius, University of California, San Francisco, San Francisco, CA; Brake et al., 1994) was subcloned into the SmaI site of pGEMHE. Single- and double-point mutants were made using a QuikChange site-directed mutagenesis kit (Agilent Technologies) and confirmed by sequencing as described previously (Fujiwara et al., 2009; Keceli and Kubo, 2009). Each subunit for tandem trimers was amplified by using unique pairs of PCR primers that had 7–12-nucleotide-long custom-made overhangs with one uracil intentionally put in. This uracil residue was excised with USER enzyme (a uracil-specific excision enzyme that is a commercial mix of uracil DNA glycosylase and DNA glycosylase-lyase

Endo VIII from New England Biolabs, Inc.) after PCR, which creates single-stranded overhangs designed to be complementary to that of the neighboring subunit to be ligated. Using this method, amplified subunits and vector ligation were successfully achieved in the desired order (Nour-Eldin et al., 2010). The pNB1u vector (provided by H.H.N. Eldin and A.N. Poulsen, University of Copenhagen, Copenhagen, Denmark) was digested with PacI and Nt.BbvCI to generate eight nucleotide overhangs. The forward and reverse primers used for amplification of the first subunit are: 5′-GGCTTAAUATGGTCCGGCGCTTGGCCCGGGGCTGCTGG-3′ and 5′-ATTACCATUGAGCTGGGCCAAACCTTTGGGGTCCG-3′. The forward and reverse primers used for amplification of the second subunit are: 5′-AATGGTAAUATGGTCCGGCGCTTGG-CCCGG-3′ and 5′-ACCUGAAAGTGGGCCAAACCTTTGGGGT-CCGT-3′. The forward and reverse primers used for amplification of the third subunit are: 5′-AACTUTCAGGUATGGTCCGGCG-CTTGGCCCGGG-3′ and 5′-GGTTTAAUTCAAAGTTGGGCCA-AACCTTTGGGGTCCGT-3′.

Gln471 and Leu472 had silent mutations (5′-CAACTT-3′→ 5′-CAGCTC) in the linker between the first and second subunits for differential recognition of sequence primers for two different linkers. The linkers between the first and the second subunits had Asn, Gly, and Asn; the linkers between the second and the third subunits had Ser and Asn amino acids in addition to the original sequence instead of a stop codon. The TTCs were confirmed by DNA sequencing. The whole trimer was sequenced part-by-part using specific primers for intersubunit linkers and also before and after cloning site of the vector. We used the universal T7 primer sequence 5′-TAATACGACTCACTATAGGG-3′ (which is ∼200 nucleotides before the first methionine) as the forward primer and a sequence from the linker between the first and second subunits, 5′-GACCATATTACCATTGAGCT-3′, as the reverse primer to read the first subunit. For the second subunit of the concatenated trimer, we used 5′-GGTTTGGCCCAGCTCAATGG-3′ for the forward primer in the linker between the first and second subunits and 5′-GCGCCGGACCATACCTGA-3′ for the reverse primer in the linker between the second and third subunits. For the third subunit, we used the forward primer 5′-TTG-GCCCAACTTTCAGGT-3′ between the second and third subunits and 5′-AGCTTAGAGACTCCATTCGG-3′ as the reverse primer, which is ∼150 nucleotides distant from the stop codon. WT, mutant, and tandem receptors were then prepared from the plasmid cDNA linearized by NheI using a T7 RNA transcription kit (Ambion) as described previously (Fujiwara et al., 2009; Keceli and Kubo, 2009).

A note about nomenclature: in this paper, we use the terms *cis* and *trans* to describe the relative orientation of mutations in the trimer to indicate whether they are on the same or adjacent subunits, respectively.

Preparation of *Xenopus laevis* oocytes
Xenopus oocytes were collected from frogs anesthetized in water containing 0.15% tricaine. After the final collection, the frogs were killed by decapitation. Isolated oocytes were treated with collagenase (2 mg ml^{-1}; type 1; Sigma-Aldrich) for 6 h, after which oocytes of similar size at stage V were injected with 50 nl of cRNA solution as described previously (Fujiwara et al., 2009; Keceli and Kubo, 2009). The injected oocytes were then incubated for 1–2 d at 17°C and moved to 4–8°C in frog Ringer's solution to avoid high expression levels. All experiments conformed to the guidelines of the Animal Care Committee of the National Institute for Physiological Sciences and were performed with an approval from the committee.

Two-electrode voltage-clamp recordings in *Xenopus* oocytes
Macroscopic currents were recorded from *Xenopus* oocytes using the two-electrode voltage-clamp technique with a bath clamp

amplifier (OC-725C; Warner Instruments) as described previously (Fujiwara et al., 2009; Keceli and Kubo, 2009). In brief, stimulation, data acquisition, and data analyses were performed on a Pentium-based computer using Digidata 1322A and pCLAMP 9.2 software (Molecular Devices). All recordings were obtained at room temperature. Intracellular glass microelectrodes were filled with 3 M potassium acetate containing 10 mM KCl, pH 7.2, and the resistances ranged from 0.1 to 0.3 MΩ. Two Ag-AgCl pellets (Warner Instruments) were used to pass the bath current and sense the bath voltage. The recording bath solution contained 95.6 mM NaCl, 1 mM MgCl$_2$, 5 mM HEPES, and 2.4 mM NaOH at pH 7.35–7.44. ATP disodium salt (Sigma-Aldrich) was dissolved in bath solution (pH 7.35). When applied to cells, a one-fifth bath volume of 5× concentrated ATP solution was pipetted into the bath. All data were recorded by applying a set of step pulses during the steady state ∼8–10 s after agonist application. Oocytes expressing relatively low levels of P2X$_2$ (ATP-evoked I of <4.0 µA at −60 mV) were used to achieve sufficiently accurate voltage clamping, to avoid changes in the properties of the channel caused by the high expression level (Fujiwara and Kubo, 2004; Fujiwara et al., 2009; Keceli and Kubo, 2009), and to avoid any cross-assembly between individual TTCs. The background leak current before ATP application was measured and subtracted to isolate the ATP-induced current. Oocytes having leak currents >0.3 µA at −40 mV were discarded.

Data analysis

Data were analyzed using Clampfit 9.2 (Molecular Devices) and Igor Pro (WaveMetrics) software as described previously (Fujiwara et al., 2009; Keceli and Kubo, 2009). The activation time constants (τ) were obtained by fitting the activation phase of the inward currents elicited upon hyperpolarization with a single-exponential function. For analysis of the G-V relationship, the inward tail current amplitudes at −60 mV were measured and fitted using Clampfit 9.2 software to fit to a two-state Boltzmann equation:

$$I = I_{min} + \frac{I_{max} - I_{min}}{1 + e^{-\frac{ZF}{RT}(V - V_{1/2})}},$$

where I$_{min}$ and I$_{max}$ are the limits of the amplitudes in the fittings, Z is the effective charge, V$_{1/2}$ (mV) is the half-activation voltage, F is Faraday's constant, R is the gas constant, and T is temperature in Kelvin. I$_{min}$ here is the inward current with the largest amplitude. Normalized G-V relationships were fitted using the following equation:

$$G/G_{max} = I/I_{min} = 1 - \left(1 + e^{-ZF(V - V_{1/2})}\right)^{-1} \left(1 - I_{max}/I_{min}\right).$$

To evaluate τ (ms), V$_{1/2}$ (mV), and Z value differences between the constructs, two-factor ANOVA was performed. Two-factor ANOVA enables simultaneous evaluation of the effects of two independent variables (simple main effects of [ATP] and construct) as well as the interaction between these variables, which reveals whether the effect of [ATP] differs between the constructs. The activation time constants for the constructs WT–WT–WT and TTCs with one, two, and three T339S mutations were evaluated using one-factor ANOVA and post-hoc multiple comparisons. Half-maximal [ATP] concentrations (EC$_{50}$) were calculated from dose–response relationships for individual oocytes by least-squares fitting to the Hill–Langmuir equation,

$$E = \sum_{i=1}^{n} \frac{\left(I_{max_i} \left[ATP\right]^{h_i}\right)}{\left(EC_{50_i}^{h_i} + \left[ATP\right]^{h_i}\right)},$$

where E is the current, n is the number of terms (constrained to two for the biphasic dose–response relationships observed in the

D315A mutant and unconstrained for others), and h is the Hill coefficient. The differences between EC$_{50}$ and Hill coefficient values for WT and WT–WT–WT were analyzed using nonparametric t tests (Mann–Whitney U). The differences between EC$_{50}$ and Hill coefficient values for WT–WT–WT and TTCs with one K308A mutation were analyzed using one-factor ANOVA and post-hoc multiple comparisons. The results of the statistical tests are reported with the obtained value of the test, degrees of freedom, and the significance level. For all statistical tests, P < 0.05 was accepted as significantly different. The details of statistical analyses of the data presented in the figures are given in the supplemental text.

ΔG values in Fig. S14 were calculated from the G-V plot data of WT–WT–WT and TTC harboring one, two, and three T339S and D315A mutants at saturating concentrations of ATP at 0 mV by ΔG = −RT ln(P/(1 − P)), where R and T are constants as mentioned before, and P is the open probability ratio from the normalized Boltzmann fitting of the maximum tail currents at −60 mV.

Three-dimensional structural modeling of rat P2X$_2$

As described previously (Keceli and Kubo, 2009), closed-state rat P2X$_2$ homology modeling used in Figs. 1 (A–D) and 11 was performed based on sequence alignment of amino acid residues 34–351 of the rat P2X$_2$ and zebra fish P2X$_4$, whose crystal structure has been solved (Kawate et al., 2009; Protein Data Bank accession no. 3I5D) by using DeepView/Swiss Protein Data Bank viewer v.4.0.1 and SWISS-MODEL (automated protein modeling server; Arnold et al., 2006; Bordoli et al., 2009; Kiefer et al., 2009). For the homology model used in Fig. 1 (E–H), we performed the homology modeling for the open state of rat P2X$_2$ based on the open-state structure of zebra fish P2X$_4$ (Hattori and Gouaux, 2012; Protein Data Bank accession no. 4DW1) and the sequence alignment of amino acid residues 34–351 of the rat P2X$_2$ and zebra fish P2X$_4$ (Hattori and Gouaux, 2012) by using DeepView/Swiss Protein Data Bank viewer v.4.0.1 and SWISS-MODEL. Graphic presentations were made using PyMOL (Schrödinger, Inc.).

Western blotting

To confirm the expression of trimeric constructs, we performed Western blotting (Fig. S1). Oocytes were frozen 3–4 d after injection of cRNA. Western blotting was performed on day 3 after injection for the analyses of the expression pattern of the test constructs used in Fig. S12 (see also Fig. S13). Frozen oocytes were sonicated in PBS containing protease inhibitor (Roche). Homogenate was centrifuged at 3,000 rpm at 4°C for 10 min to remove yolk, and the resultant supernatant was used as a whole protein extract. Western blotting of whole protein extracts was performed using an affinity-purified anti-P2X$_2$ rabbit antibody (Sigma-Aldrich). The region used as immunogen corresponds to amino acids 457–472 of rat P2X$_2$, with an additional N-terminal cysteine. Successful expression of trimeric construct proteins was confirmed.

Simulation study by Markov model

For the models depicted in Fig. 10 (A–C), we performed simulations using the Q-matrix method (Colquhoun and Hawkes, 2009). Q-matrix (Q) was established with the assumption that conformational rearrangements of each subunit from closed to open have three main steps with two transitions: a fast ATP-binding step and a rate-limiting voltage-dependent gating step as shown in Fig. 10 A (bottom left). For each binding and unbinding event, we used the rate constants k$_{bind}$ = 2.6 × 10^7 [M^{-1} · s^{-1}] and k$_{unbind}$ = 1.1 × 10^3 [s^{-1}] as used in previous works (Fujiwara et al., 2009; Keceli and Kubo, 2009), which were determined with reference to the single-channel analysis (Ding and Sachs, 1999). Voltage-dependent gating step rate constants k$_{on}$ and k$_{off}$ were obtained similarly as previously discussed (Fujiwara et al., 2009; Keceli and Kubo, 2009) using experimentally obtained β and α from macroscopic recordings at various voltages from k$_{on}$ = ((1 + Kd)/[ATP]) × β and

$k_{off} = \alpha$. The dissociation constant value is taken as constant at 42 µM and not voltage dependent (Ding and Sachs, 1999). Calculated k_{on} and k_{off} values at −60 and −160 mV are as follows: for k_{on}, [33.5, 56.3] (s^{-1}); for k_{off}, [14.8, 3.9] (s^{-1}). For each membrane potential and for various [ATP] concentrations, Q-matrices were constructed corresponding to the depicted models shown in Fig. 10. In Q-matrix (Q), each element q (i, j) (i ≠ j) is the transition rate (s^{-1}) for the transition from state i to j. Diagonal elements, q (i, i) were constructed so as to make each row sum to zero. The equilibrium occupancies are found by using matrix augmentation as described previously (Hawkes and Sykes, 1990; Colquhoun and Hawkes, 2009). We augmented Q by a unit column u matrix to the right-hand end of Q to produce a matrix with k rows and k + 1 columns, and called this matrix S. The solution for the equilibrium occupancies was calculated as $p(\infty) = u^T(SS^T)^{-1}$, in which S^T represents the transpose of S, and SS^T is a matrix with k rows and k columns (Hawkes and Sykes, 1990; Colquhoun and Hawkes, 2009). State occupancy at time (t) was calculated as,

$$p(t) = p(0)e^{Qt},$$

where p(t) is a row vector corresponding to occupancy of each state in the model at time (t), and e^{Qt} is the transition probability matrix, which can be conveniently calculated using the spectral expansion (Colquhoun and Hawkes, 2009),

$$e^{Qt} = \sum_{i=2}^{k} A_i e^{(-\lambda_i t)},$$

where λ_i is eigenvalues of the matrix −Q, k is the number of states, and A_i is a set of square matrices derived from Q and known as spectral matrices of Q. To get the macroscopic response to a sudden voltage change from −60 mV steady state to −160 mV at various [ATP], we calculated the spectral expansion of the matrix exponential e^{Qt} as,

$$p(t) = p(\infty) + p(0) \sum_{i=2}^{k} A_i e^{(-t/\tau_i)},$$

where $\tau_i = 1/\lambda$ is the time constant of ith component. p(0) here is the steady-state occupancy at −60 mV. We denote as p(t) the fraction of channels that are referred to as the occupancy.

Therefore, in general terms, the current is I(t) = N p(t) γ (V − Vrev), where N is the number of channels, γ is a column vector that defines conductance of a single open channel (Siemens), and (V − Vrev) is the driving force (volts). Finally, time courses of the activation traces at various [ATP] (from 3 to 300 µM) were normalized. Single-exponential fitting is performed for the activation traces of each simulation in response to 3 µM ATP. MathCad2001 was used to solve the equations of simulations modeled.

Online supplemental material

The online supplemental material contains 14 figures and text for the detailed statistical analyses to compare the quantitative parameters of the voltage- and [ATP]-dependent gating of different constructs. Fig. S1 shows the expression of the three-tandem repeat proteins analyzed by Western blotting. Fig. S2 illustrates the representative macroscopic current recordings of WT, WT–WT–WT, WT–K308A–WT, and K308A–K308A–WT. Fig. S3 shows the representative macroscopic recordings of K308A–WT–WT and WT–WT–K308A. Fig. S4 indicates that one ATP-binding site mutation (K308A) in the TTC does not have a position effect for voltage- and [ATP]-dependent gating. Fig. S5 illustrates representative macroscopic recordings from the D315A mutation at the linker region. Fig. S6 shows the representative macroscopic recordings of tandem trimers with three, two, and one D315A mutant

subunits. Fig. S7 illustrates representative macroscopic recordings of *trans* (K308A–D315A–WT) and *cis* (WT–K308A&D315A–WT) tandem trimers. Fig. S8 shows the analyses of the order of individual subunits in tandem trimers using simultaneous K308A and K69A mutations. Fig. S9 illustrates the representative macroscopic recordings of D315A&K69A–WT–WT and WT–D315A–K69A. Fig. S10 shows representative macroscopic recordings of *trans* and *cis* constructs K308A–T339S–WT and WT–K308A&T339S–WT. Fig. S11 illustrates representative macroscopic recordings of *trans* and *cis* constructs D315A–T339S–WT and WT–D315A&T339S–WT. Fig. S12 indicates that hetero assembly between individual subunits of tandem trimers is very unlikely in our experimental protocol where very low expression levels are used. Fig. S13 indicates that the expression level of experimental constructs in Fig. S12 is not lower, and is even higher, than other constructs via Western blotting. Fig. S14 indicates that subunit cooperativity is different at linker and pore domains by the analyses of the free energy (ΔΓ, kcal/mol) changes at 0 mV at the saturating concentrations of ATP, as a function of the number of T339S and D315A mutations in the trimer. The online supplemental material is available at http://www.jgp.org/cgi/content/full/jgp.201411166/DC1.

RESULTS

Voltage- and ATP-dependent gating of P2X$_2$ can be observed with two ATP molecules bound but not one

We first confirmed that the functional properties of the TTC of WT subunits (WT–WT–WT) are similar to WT in terms of voltage- and [ATP]-dependent gating. As shown in Fig. S2 (A and B), the representative voltage-induced activation traces of the WT–WT–WT tandem trimeric structure are highly similar to WT, with a single-exponential hyperpolarization-induced activation.

To evaluate the exact number of bound ATP molecules that is sufficient and essential for activation of the P2X$_2$ receptor channel, we made TTCs with one or two K308A mutations (Fig. 1) that eliminate ATP binding (Jiang et al., 2000). We observed that voltage- and [ATP]-dependent gating of the P2X$_2$ receptor channel was still intact upon removing one of the three ATP-binding sites but was abolished with the removal of two binding sites (Fig. S2, C and D). As shown in Fig. S2 C, WT–K308A–WT responses were very similar to WT and WT–WT–WT in terms of the presence of single-exponential voltage-induced activation traces upon hyperpolarizing step pulses. We also observed a similar phenotype when inserting the K308A mutation into different subunits in the trimer (Fig. S3, A and B).

Normalized voltage-induced activation traces from −40 to −160 mV after the application of various [ATP] were very similar for WT, WT–WT–WT, and WT–K308A–WT, as shown in Fig. 2 A. With the increase in [ATP], the kinetics of hyperpolarization-induced activation was accelerated similarly in all three constructs (Fig. 2 A), as well as in K308A–WT–WT and WT–WT–K308A (Fig. S4 A). To analyze voltage-induced activation time constants of the constructs (Fig. 2 B), we evaluated the time constants at a −160-mV membrane potential at various [ATP]. We analyzed the time constants of WT and WT–WT–WT

by two-factor ANOVA. The results showed that activation time constants of WT–WT–WT were similar to WT protomer at identical [ATP], with no significant statistical difference (P > 0.05; for details see the supplemental text). As the next step, time constants at a −160-mV membrane potential at various [ATP] were compared for the WT–WT–WT and TTCs with one K308A mutation (Figs. 2 B and S4 B) using two-factor ANOVA. The results showed that activation time constants at identical [ATP] for WT–WT–WT and TTCs with one K308A were similar, with no significant statistical difference (P > 0.05; for details see the supplemental text). In summary, voltage-induced activation time constants calculated from the fittings of the voltage-induced activation phases with a single-exponential function at various [ATP] and membrane potentials were highly similar in all of these constructs (Figs. 2 B and S4 B; details of the statistical analyses are in the supplemental text).

Analysis of the tail currents with only two intact ATP-binding sites revealed a concentration-dependent G-V shift to depolarized potentials, as observed in WT (Figs. 2 C and S4 C). The results showed that TTCs with a single ATP-binding site block had a G-V shift to depolarized potentials in increasing [ATP], as observed in WT and WT–WT–WT. The constructs also showed [ATP]-dependent $V_{1/2}$ (mV) changes, as observed in WT and WT–WT–WT. The [ATP]-dependent $V_{1/2}$ (mV) and Z value changes were not significantly different among the constructs, and there was no significant position effect for TTCs with K308A at different subunits (Fig. S4 D; details of the statistical analyses are in the supplemental text).

We also analyzed the dose–response relationships for WT, WT–WT–WT, and TTC with K308A mutations at different subunits in the trimer. [ATP] dose–response relationships at −160 mV for K308A–WT–WT, WT–K308A–WT, and WT–WT–K308A together with WT and WT–WT–WT are shown in Fig. 2 D. Mean EC_{50} values and Hill coefficients are shown in Fig. 2 (E and F).
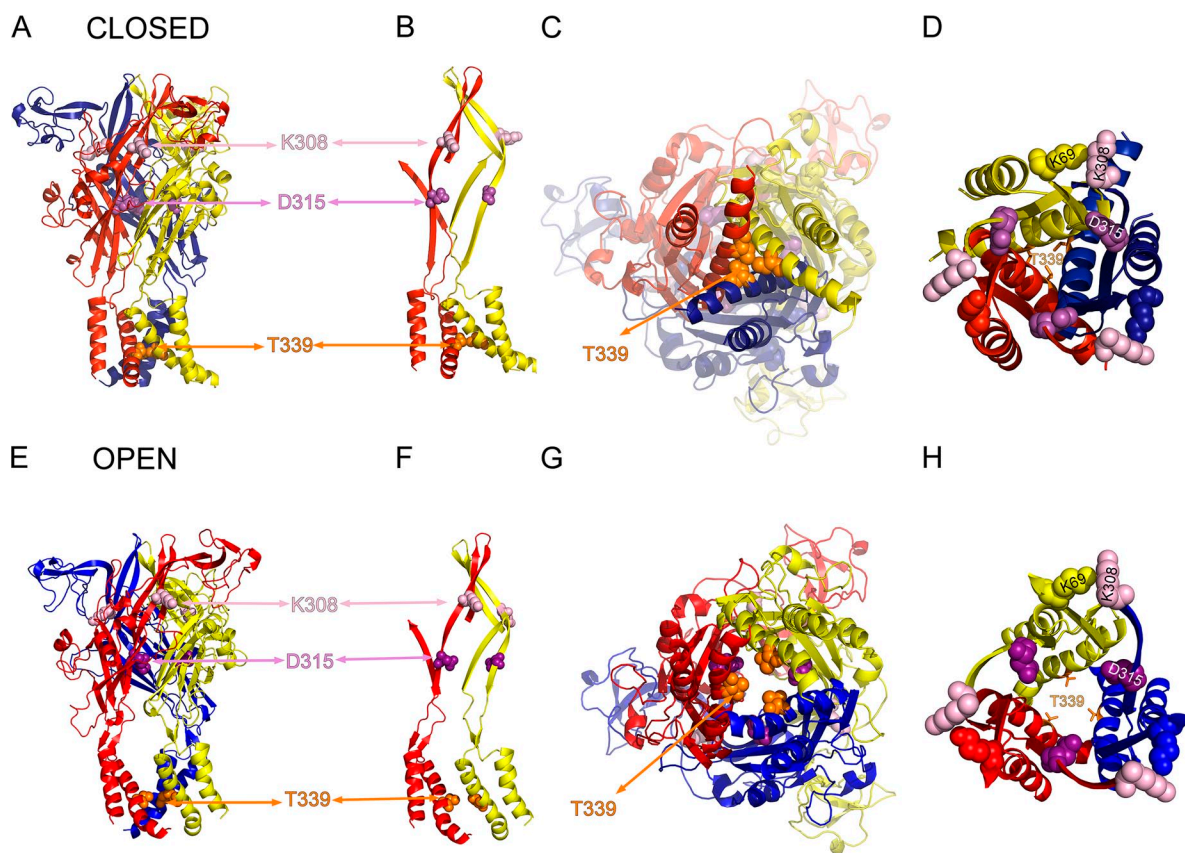
Figure 1. Homology modeling of the structure of rat P2X$_2$ from zebra fish P2X$_4$ in closed and open states with localization of the residues K308, D315, and T339S, which are critical in the homotrimer for voltage- and [ATP]–dependent gating. (A and E) Homology model of the rat P2X$_2$ structure based on the closed- (A) and open-state (E) structures of zebra fish P2X$_4$ (Kawate et al., 2009; Hattori and Gouaux, 2012). The critical residues at the ATP-binding site (K308), linker (D315), and pore (T339) are shown in pink, magenta, and orange spheres, respectively. (B and F) Only the TM helices and their connections to ATP-binding sites are shown for a better view of critical residues in closed (B) and open (F) states. (C and G) Bottom views of the pore in closed (C) and open (G) states showing T339 residues. (D and H) Top view just above the level of the intersubunit ATP-binding site in closed (D) and open (H) states. K308 and K69 form a groove for the intersubunit ATP docking.

Our results for the [ATP] dose–response relationship analysis showed that removal of one ATP-binding site caused a slight change in the efficiency of channel activation, which was only significant for K308A–WT–WT.

We did not observe any major position effect in the dose–response relationships for TTCs with removal of one ATP-binding site (Fig. 2 E; details of the statistical analyses are given in the supplemental text).
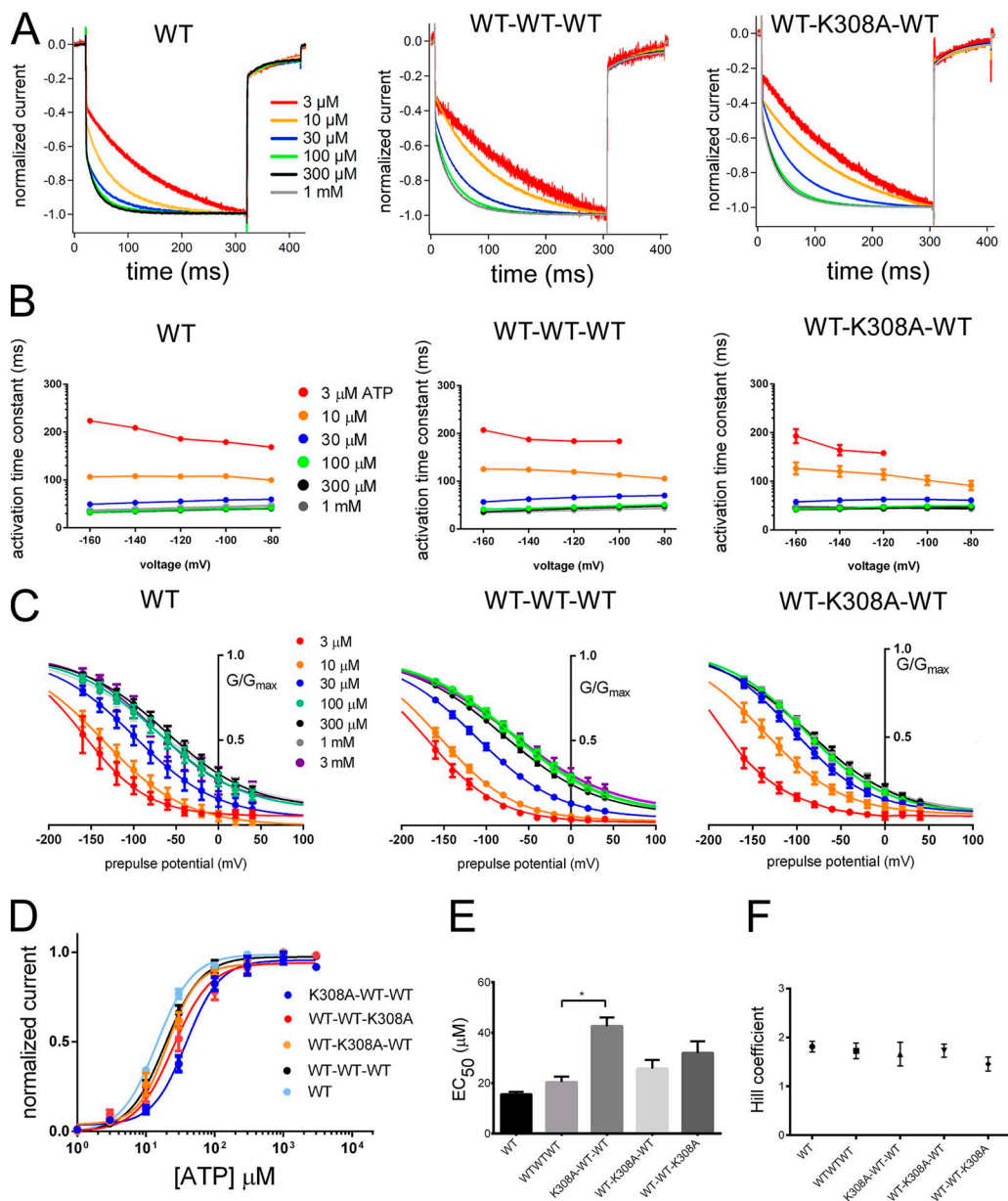
Figure 2. Analysis of voltage- and ATP-dependent gating for WT, WT–WT–WT, and WT–K308A–WT. Voltage- and [ATP]-dependent gating is intact when one ATP-binding site is disrupted. (A) Normalized voltage-induced activation traces for WT, WT–WT–WT, and WT–K308A–WT from the representative data shown in Fig. S2 at −160 mV at various concentrations of ATP. (B) Mean (± SEM) of activation time constants at various [ATP] and membrane potentials for WT ($n = 7$–9), WT–WT–WT ($n = 12$–18), and WT–K308A–WT ($n = 8$–25) at various [ATP]. (C) Mean (± SEM) normalized G-V relationship for WT ($n = 9$), WT–WT–WT ($n = 26$), and WT–K308A–WT ($n = 12$) derived from the maximum tail current responses by fitting with the two-state Boltzmann equation as described in Materials and methods. (D) Mean (± SEM) [ATP] dose–response relationships at −160 mV for K308A–WT–WT ($n = 6$), WT–K308A–WT ($n = 13$), and WT–WT–K308A ($n = 11$), together with WT ($n = 16$) and WT–WT–WT ($n = 10$). (E) Mean (± SEM) EC_{50} values and (F) Hill coefficients are derived from the fitting of the normalized maximum [ATP] dose–response relationships in D with the Hill equation. Mean (± SEM) EC_{50} values for WT ($n = 16$), WT–WT–WT ($n = 10$), K308A–WT–WT ($n = 5$), WT–K308A–WT ($n = 12$), and WT–WT–K308A ($n = 11$) are 14.5 ± 1.2 µM, 19.1 ± 2.0 µM, 42.3 ± 2.2 µM, 22.9 ± 1.8 µM, and 33.3 ± 1.65 µM, respectively. Mean (± SEM) Hill coefficients for WT ($n = 16$), WT–WT–WT ($n = 10$), K308A–WT–WT ($n = 5$), WT–K308A–WT ($n = 13$), and WT–WT–K308A ($n = 11$) are 1.7 ± 0.2, 1.8 ± 0.2, 1.7 ± 0.18, 1.8 ± 0.18, and 1.6 ± 1.4, respectively. *, $P < 0.05$.

In summary, our overall results indicate that the removal of one ATP-binding site with one K308A mutation conserved the general phenotype for voltage-dependent gating, namely [ATP]-dependent acceleration in voltage-dependent gating kinetics and a G-V curve shift to depolarized potentials (Fujiwara et al., 2009; Keceli and Kubo, 2009).

D315A mutation in the linker region on β-*14* strand creates two different gating modes

We observed that the D315A mutation in the linker region, which is on the β-*14* strand linking the ATP-binding region to the pore-harboring TM2 helices, resulted in two different gating modes depending on ATP concentration (Figs. S5 and 3). Representative traces of D315A (Fig. S5) are clearly different from WT (Fig. S2 A). At low [ATP], activation was not clearly voltage dependent, and at relatively higher [ATP], it showed clear voltage dependence (Fig. S5). The D315A mutant revealed a biphasic dose–response relationship at −160 mV (Fig. 3 A). When we analyzed the dose–response relationships at various voltage steps from −60 to −160 mV, we observed an apparent voltage-dependent shift of the dose–response relationship in the second phase but not in the first phase (Fig. 3 B). We also analyzed the tail currents (Fig. 3 C) and voltage-induced activation

phases (Fig. 3 D) at various [ATP] for D315A in which the two different gating modes were apparent. For D315A, G-V relationships were different at low and high [ATP]; the channel was equally active at every membrane potential at low [ATP], and at relatively higher [ATP], the channel started to show voltage-dependent conductance changes (Fig. 3 C). Similarly, normalized voltage-induced activation phases at various potentials (Fig. 3 D) showed no voltage-dependent activation at low [ATP] and an exponential voltage-dependent activation at higher [ATP]. The D315A mutation on the linker strand between the ATP-binding site and pore-forming TM2 helices changed the channel gating dramatically to create two different gating modes characterized by the absence and presence of the voltage-induced activation phase at low and high [ATP], respectively. We used this unique effect of the D315A mutation for our further analysis of the activation signal transmission from the ATP-binding site to the pore level.

At least two subunits are required to have the D315A mutation to produce two different gating modes

The D315A mutation appears to be a useful tool to analyze how each intersubunit ATP-binding event will transmit its activation signal down to the pore, and how individual subunits affect each other. We further analyzed
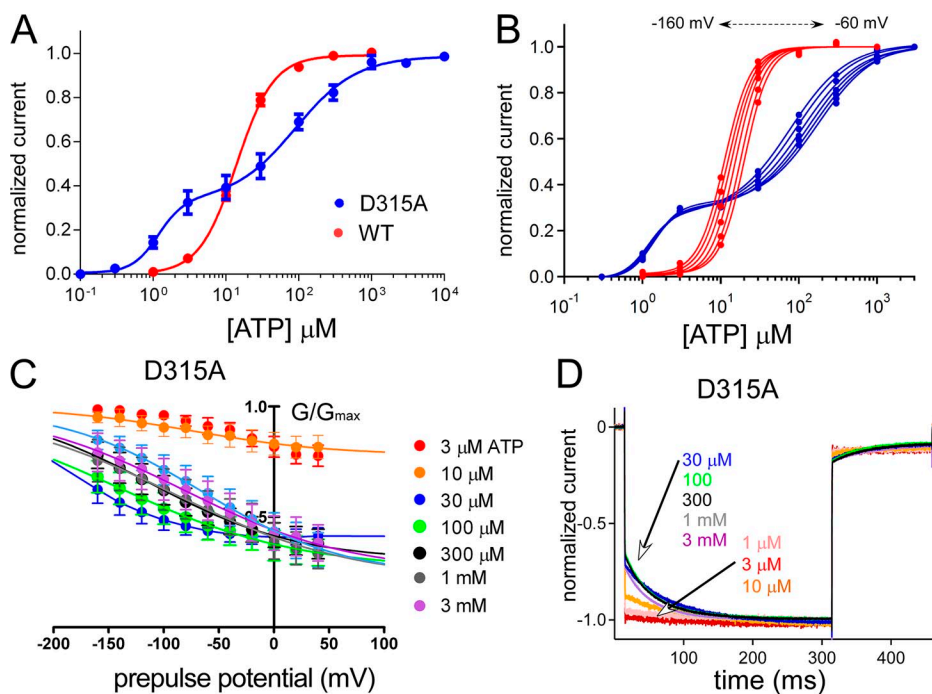
Figure 3. Analysis of voltage- and [ATP]-dependent gating of the $P2X_2$ receptor channel with the D315A mutation in the linker region. The D315A mutation reveals two different gating modes. (A) Mean (± SEM) [ATP] dose–response relationships for WT and D315A at −160 mV are shown in red and blue, respectively. EC_{50} (1) and EC_{50} (2) for D315A are $1.2 ± 0.6$ μM and $89.1 ± 1.48$ μM, with Hill coefficients of Hill (1) = $2.4 ± 0.7$ and Hill (2) = $1.0 ± 0.2$ ($n = 10$). EC_{50} for WT is $14.5 ± 1.2$ μM with a Hill coefficient of $1.7 ± 0.2$ ($n = 16$). (B) [ATP] dose–response relationship from a single representative experiment for WT (red) and D315A (blue). A dose–response shift by voltage is observed for WT and only for the second phase of D315A at high [ATP]. (C) Mean (± SEM) normalized G-V relationship at various [ATP] for D315A ($n = 8$) derived from the maximum tail current responses by fitting with the two-state Boltzmann equation, as described in Materials and methods. (D) Normalized voltage-induced activation traces for D315A at −160 mV at various concentrations of ATP from the representative traces shown in Fig. S5.

the effect of D315A by preparing TTCs having the D315A mutation in one, two, or three subunits. When inserted into a single subunit in the trimer, the D315A mutation did not change voltage- and [ATP]-dependent gating and showed a phenotype similar to WT (Fig. S6). However, when D315A was introduced into two or three subunits, the phenotypes of the mutants were different from WT but similar to each other, with two phases in the [ATP] dose–response relationship at −160 mV (Fig. 4 A). The first phase did not show a clear voltage-dependent shift (Fig. 4 B), whereas in the second phase, there was an apparent voltage-dependent shift (Fig. 4 B). The G-V curves of trimers with two or three D315A (D315A–D315A–D315A and D315A–D315A–WT) showed that the

channel became equally active at every membrane potential at low [ATP], and that at high [ATP], voltage-dependent conductance changes started to appear (Fig. 4 C).

The trimer having only one D315A (D315A–WT–WT) showed voltage-dependent conductance changes even at low [ATP] and G-V curve shifts to depolarized potentials with increased [ATP], which shows that the WT phenotype was conserved (Fig. 4 C). In Fig. 4 D, normalized voltage-induced activation phases in the steady state after various [ATP] applications are shown. Trimers with two or three D315A mutants showed no voltage-induced activation phases at low [ATP]. However, trimers with only one D315A mutation showed an exponential voltage-induced activation phase at every [ATP]
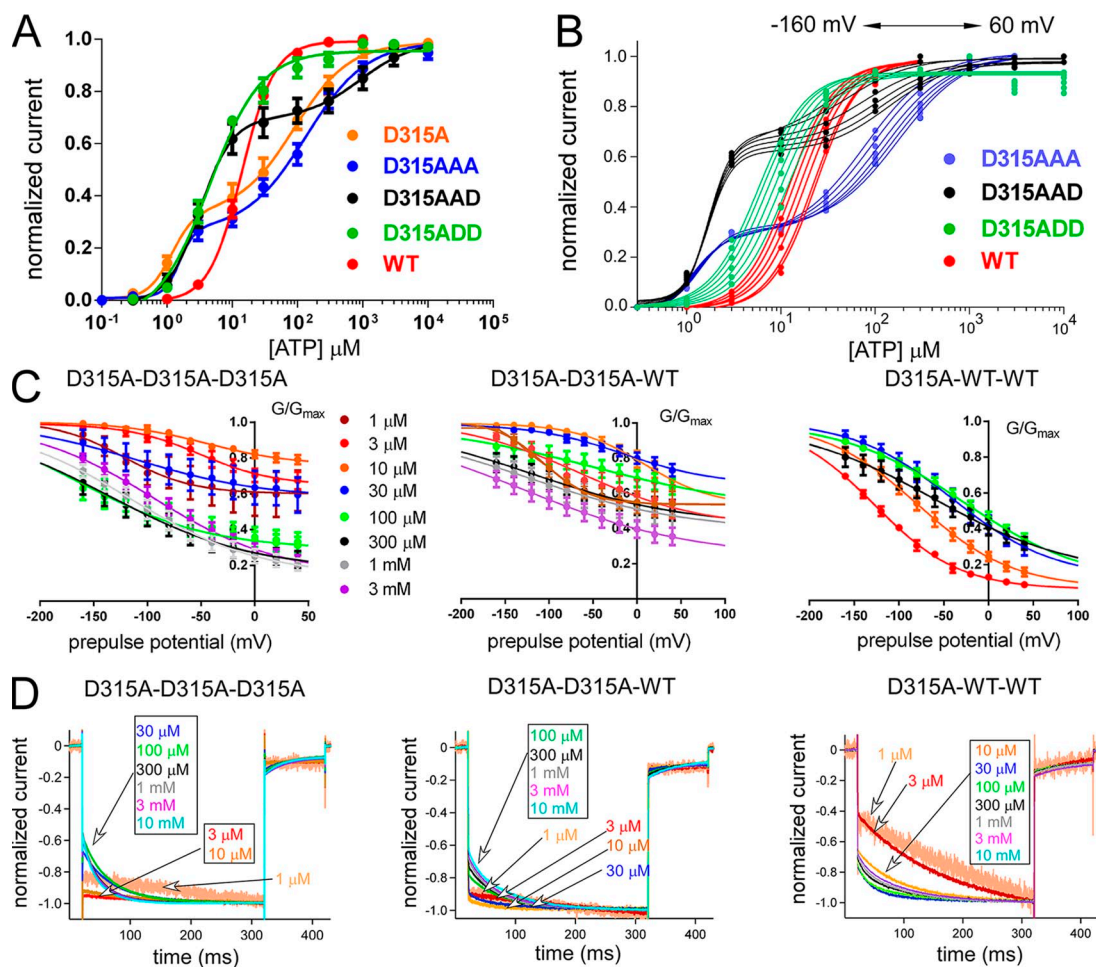
Figure 4. Analysis of voltage- and [ATP]-dependent gating of tandem trimers having three, two, and one D315A mutant subunits. Two subunits with D315 are necessary for normal gating. (A) [ATP] dose–response relationships at −160 mV for WT, D315A, and tandem trimers with three, two, and one D315A at various membrane potentials. Mean (± SEM) EC_{50} values and Hill coefficients are as follows: WT: EC_{50}, 14.5 ± 1.2 µM, and Hill, 1.7 ± 0.2 ($n = 16$); D315A–D315A–D315A: EC_{50} (1), 1.5 ± 0.8 µM; EC_{50} (2), 130 ± 5.0 µM; Hill (1), 3.7 ± 0.6; and Hill (2), 1 ± 0.2 ($n = 13$); D315A–D315A–WT: EC_{50} (1), 3.15 ± 0.9 µM; EC_{50} (2), 794 ± 12 µM; Hill (1), 1.8 ± 0.2; and Hill (2), 1.06 ± 0.2 ($n = 22$); and D315A–WT–WT: EC_{50}, 6.02 ± 1.1 µM, and Hill, 1.4 ± 0.1 ($n = 24$). (B) One representative experiment from tandems of D315A and WT to show the shift of dose–response relationships by voltage in between −60 to −160 mV. (C) Cumulative data for normalized G-V relationships at various [ATP] for tandem trimers with three ($n = 8$), two ($n = 8$), and one ($n = 6$) D315A mutant subunit, derived from the maximum tail current responses by fitting with the two-state Boltzmann equation, as described in Materials and methods. Data points are mean ± SEM. (D) Normalized voltage-induced activation traces for tandem trimers with three, two, and one D315A mutant subunit at −160 mV at various concentrations of ATP from the representative traces shown in Fig. S6.

and acceleration in voltage-dependent gating with increased [ATP] (Fig. 4 D). This phenotype is highly similar to WT and WT–WT–WT (Fig. 2).

The results showed that the presence of at least two D315A mutations in the trimer is required to observe two different gating modes. Similarly, two intact D315 residues are required to observe the WT phenotype.

T339S mutation at the pore level shows gradual changes from WT with increasing mutation number in the trimer

The P2X$_2$ pore is formed by three TM2 helices, each of which belongs to one individual subunit of the trimeric

P2X$_2$ structure (Kawate et al., 2009; Hattori and Gouaux, 2012; Fig. 1). The T339 residue is located on TM2 at the narrowest part of the pore. The T339S mutation drastically changes the gating behavior, which would be useful to assess the contribution of individual subunits to gate at the pore level. The T339S mutant does not show voltage-dependent gating and lacks the exponential voltage-induced activation at high [ATP] (Keceli and Kubo, 2009).

When the T339S mutation was introduced into all three subunits of the TTC, the P2X$_2$ receptor channel showed no voltage-dependent activation (Fig. 5 A). Tail
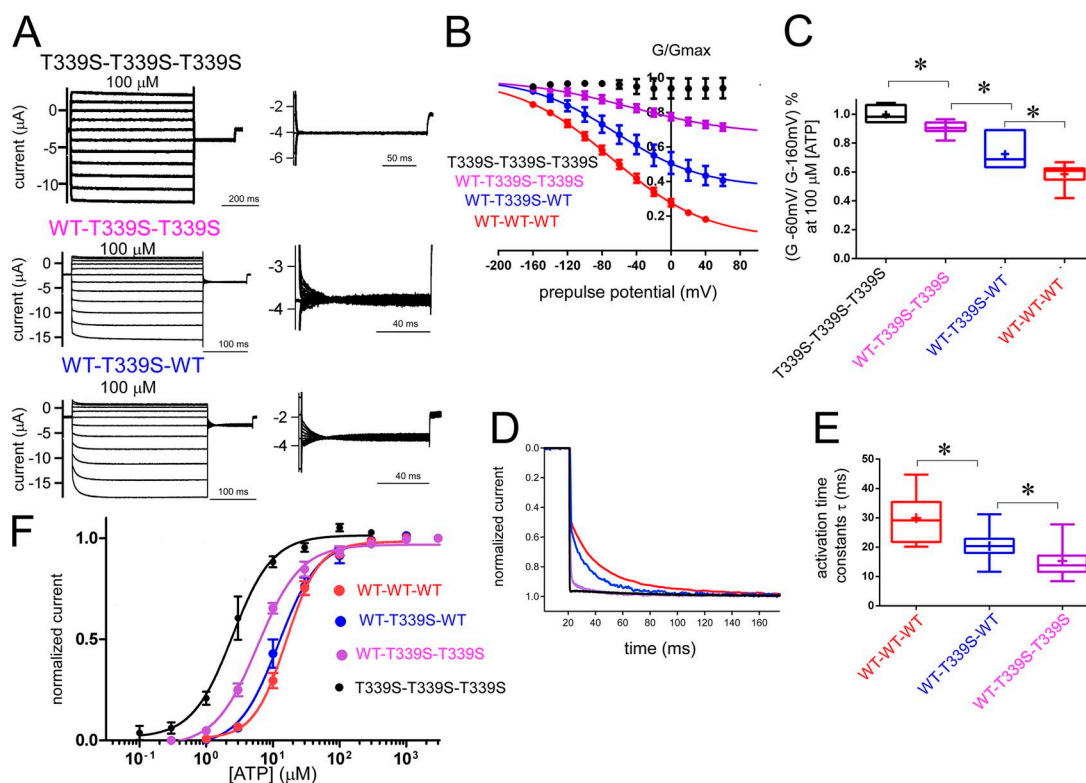
Figure 5. Analysis of voltage- and [ATP]-dependent gating of tandem trimers with three, two, and one T339S mutant subunit in the pore region of the P2X$_2$ receptor channel together with WT–WT–WT. An increase in the number of T339S in the trimer had a gradual and additive effect on voltage-dependent gating. (A) Representative macroscopic current recordings from tandem trimers with three, two, and one T339S, evoked by step pulses during the steady state after the application of saturating concentrations of [ATP]. The holding potential was −40 mV. Step pulses from 40 to −160 mV were applied in 20-mV decrements. Tail currents were recorded at −60 mV, and their enlarged images are shown next to the main activation traces. (B) Normalized G-V relationships derived from maximum tail currents at −60 mV fitted with the two-state Boltzmann equation are shown as mean ± SEM at 100 µM [ATP] for WT–WT–WT (red; $n = 12$), WT–T339S–WT (blue; $n = 9$), WT–T339S–T339S (magenta; $n = 11$), and T339S–T339S–T339S (black; $n = 6$). (C) Ratio of conductance at −60 and −160 mV at 100 µM [ATP] for tandems having three, two, and one T339S mutant subunit and WT–WT–WT is shown by a boxplot using the same color code as in B. Means are shown by a plus sign. The bottom of each box is the 25th percentile, the top is the 75th percentile, and the line in the middle is the median. Whiskers show the minimum and maximum data. *, P < 0.05. (D) Normalized voltage-induced activation traces for tandem trimers with one, two, and three T339S mutation(s) and WT–WT–WT at −160 mV at various concentrations of ATP from the representative traces shown in A (color code is the same as in C). (E) Comparisons of activation time constants at saturating concentrations of ATP for WT–WT–WT ($n = 20$) and tandem trimers with two ($n = 35$) and one ($n = 25$) T339S mutations by fitting the voltage-induced activation phase to a single-exponential function, as explained in Materials and methods. Data are shown by boxplot as in C, using the same color code. *, P < 0.05. As there is no voltage-induced activation for the tandem trimer with three T339S subunits, it was not analyzed. (F) [ATP] dose–response relationships for tandem trimers at −160 mV. EC$_{50}$ and Hill coefficients are as follows: T339S–T339S–T339S: EC$_{50}$, 2.4 ± 0.4 µM, and Hill, 1.5 ± 0.3 ($n = 7$); WT–T339S–T339S: EC$_{50}$, 6.0 ± 0.4 µM, and Hill, 1.5 ± 0.2 ($n = 10$); and WT–T339S–WT: EC$_{50}$, 12.2 ± 1.2 µM, and Hill, 1.5 ± 0.9 ($n = 6$; color code is the same as in B).

current analysis revealed that the channel was equally active at every membrane potential. The results from tandem trimers with three T339S subunits were similar to the results from T339S protomers (Keceli and Kubo, 2009). However, the macroscopic recordings showed that the voltage-induced activation phase became apparent as the number of T339S mutations in the trimer decreased (Fig. 5 A). Tail current analysis in 100 μM [ATP] (saturating concentrations of [ATP]) revealed that as the number of T339S mutations in the TTCs decreased from three to one, voltage-induced conductance differences were gradually restored (Fig. 5 B).

We also measured the ratio of instantaneous activation in response to a hyperpolarizing step pulse from −60 to −160 mV in the steady state at 100 μM [ATP] (Fig. 5 C). For TTCs with three T339S mutations, the ratio of conductance at −60 and −160 mV was close to 1, whereas the ratio showed a gradual decrease for TTCs with two, one, and zero (WT) T339S mutations (Fig. 5 C). Analyses of the voltage-induced activation time constants also showed gradual acceleration with the increase of the T339S in the trimer (Fig. 5, D and E; details of the statistical analyses are in the supplemental text).
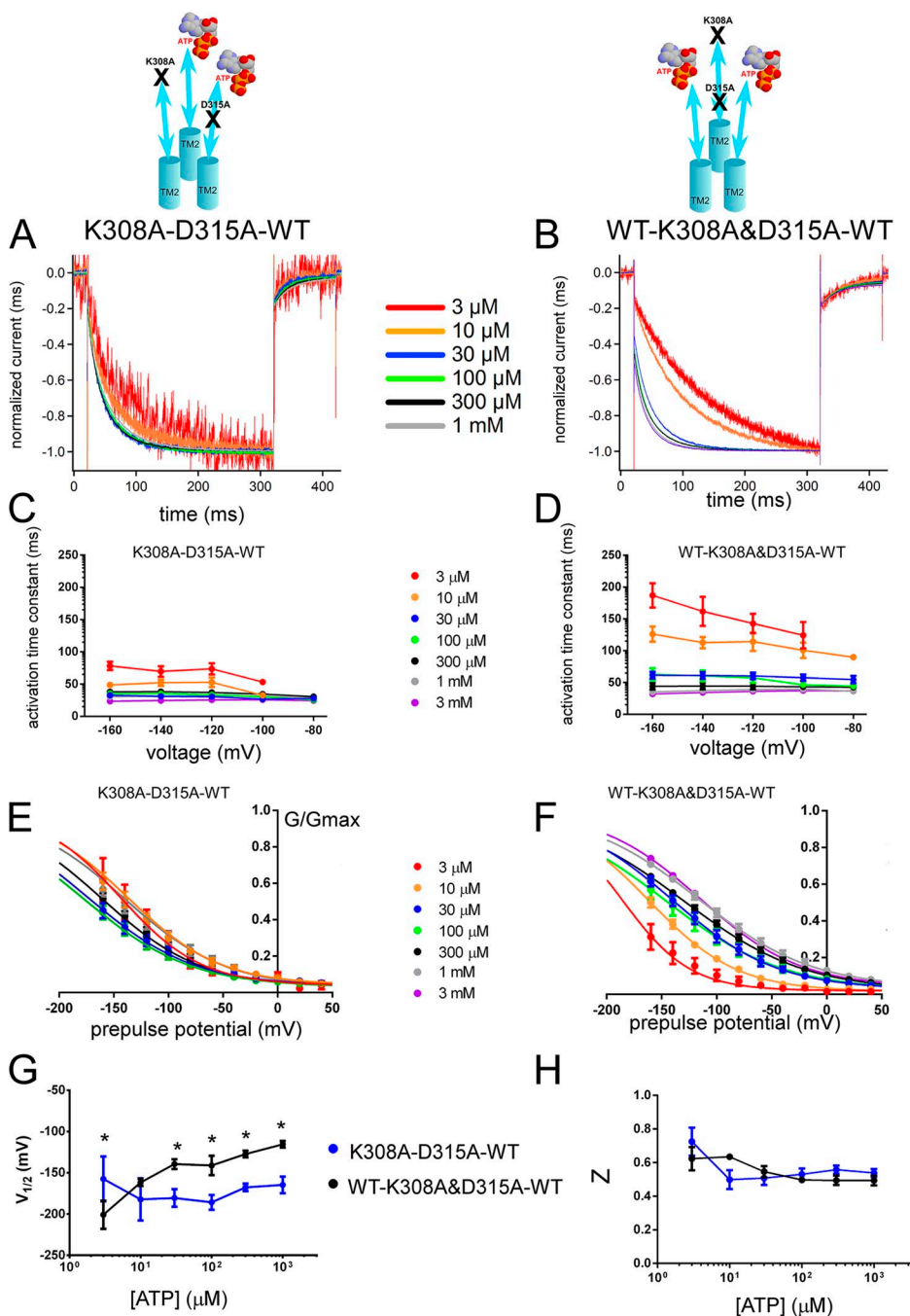
Figure 6. Voltage- and [ATP]-dependent gating differs depending on the location of one D315A relative to the location of K308A in a trimer with two intact ATP-binding sites. Analysis of *trans* (K308A–D315A–WT) and *cis* (WT–K308A&D315A–WT) constructs shows different voltage- and [ATP]-dependent gating. (A and B) Voltage-induced normalized activation traces at −160 mV of *trans* (K308A–D315A–WT; A) and *cis* (WT–K308A&D315A–WT; B) at various [ATP] from the representative data shown in Fig. S7. (C and D) Dependence of the activation time constants on voltage and [ATP] for *trans* (C) and *cis* (D) constructs. Mean (± SEM) activation time constants for *trans* (C; $n = 8–15$) and *cis* (D; $n = 14–19$) constructs at various [ATP] and membrane potentials are shown. (E and F) Normalized G-V relationship at various [ATP] for tandem trimer *trans* ($n = 9–20$; E) and *cis* ($n = 8–11$; F) derived from the maximum tail current responses at −60 mV by fitting with the two-state Boltzmann equation, as described in Materials and methods from the same oocytes. (G and H) Mean ± SEM of $V_{1/2}$ (mV) (G) and Z (H) values for the *trans* ($n = 9–20$) and *cis* ($n = 8–11$) constructs. *, $P < 0.05$.

Overall results showed that the T339S mutation at the pore level causes gradual changes as the number of mutations in the TTC increases, which suggests that at the pore level, each subunit contributes to the final pore opening equally.

Voltage- and [ATP]-dependent gating differs depending on the relative location of one D315A with respect to K308A in the trimer with two intact ATP-binding sites

When we review our results up to this point in terms of the hierarchy of the activation signal, we show that two intact ATP-binding and linker regions are necessary and sufficient for the normal signal transmission from ATP binding to the pore. However, at the pore level, there is equal contribution of each of the three subunits to the final pore opening.

As two ATP-binding sites are necessary and sufficient for voltage- and [ATP]-dependent gating of the P2X$_2$ receptor channel, we investigated how the activation signal is transmitted down to the pore level through the linker strands using K308A and D315A mutants.

We introduced a single D315A and a single K308A mutation into the trimer either on the same subunit (*cis* configuration) or on an adjacent subunit (*trans* configuration), and analyzed the voltage- and [ATP]-dependent gating (Fig. 6). In *cis* configuration, the activation signals from two intact ATP-binding sites will not encounter any direct effect of the D315A mutation, which is structurally linked to the mutated ATP-binding site. On the other hand, in *trans* configuration, one of the two activation signals would be directly affected by D315A, which is structurally linked to one of the intact ATP-binding sites. Comparison of *cis* and *trans* constructs for voltage- and [ATP]-dependent gating is expected to provide us with information about the activation signal route from two intact ATP-binding sites to the linker level.

The trimeric constructs K308A–D315A–WT (*trans*) and WT–K308A&D315A–WT (*cis*) showed voltage-dependent gating (Fig. S7). Detailed analysis of the tail currents and voltage-induced activation traces revealed differences between *cis* and *trans* configurations, suggesting that the relative position of D315A and K308A is critical for the signal transmission from ATP binding to pore opening. As shown in Fig. 6 A, normalized voltage-induced activation traces at −160 mV revealed a fast activation phase in *trans* configuration (K308A–D315A–WT), even at the lowest activating concentrations of ATP, and did not show apparent acceleration with increasing [ATP]. However, the *cis* configuration (WT–K308A&D315A–WT) showed clear acceleration in voltage-dependent activation with increasing [ATP] (Fig. 6 B). We also analyzed different combinations of *trans* constructs WT–D315A–K308A and D315A–K308A–WT to compare with K308A–D315A–WT for any possible position effect. All of the *trans* constructs were similar to each other without

any apparent [ATP]-dependent acceleration of the voltage-induced activation kinetics and G-V shift to depolarized potentials and, obviously, different from WT–K308A&D315A–WT and WT–WT–WT (not depicted).

Activation time constants calculated by single-exponential fittings of the voltage-induced traces are shown in Fig. 6 (C and D). The results showed that the activation time constants of *cis* configuration were different from the *trans* configuration. Furthermore, the effect of increasing [ATP] on the voltage-induced activation speed of the *cis* construct was different from the *trans* construct (details of the statistical analyses are in the supplemental text).

Analysis of the tail currents at various [ATP] also revealed clear differences for the G-V relationship. The *trans* configuration had a significant shift to hyperpolarized potentials compared with the *cis* configuration (Fig. 6, E–H; details of the statistical analyses are in the supplemental text). It is noteworthy that both acceleration of the voltage-induced activation phase and G-V curve shift to depolarized potentials of the *cis* configuration (WT–K308A&D315A–WT) were highly similar to WT–K308A–WT (Figs. 2 and 3). There was no apparent [ATP]-dependent G-V curve shift to depolarized potentials or acceleration in gating kinetics for the *trans* configuration.

In summary, the results show that the location of one D315A relative to the defective ATP-binding site in the TTC influenced gating, suggesting that the ATP-binding signal is directly transmitted on the corresponding β-*14* strand down to the level of D315.

Evaluation of the effect of D315A relative to a single K69A mutation in the ATP-binding site

The location of one D315A in the trimer relative to one K308A influenced the voltage- and [ATP]-dependent gating. It is of interest whether this effect is caused by the removal of one ATP-binding site relative to the location of one D315A in the trimer, or just specific to the K308A mutation used for disruption of ATP binding. For this purpose, we analyzed the effect of one D315A in the trimer where one K69A was used instead of K308A for removing ATP binding.

Because K69 and K308 are located on adjacent subunits at the ATP-binding pocket, it is important to determine the order of subunits in our TTCs to make the relative locations of K69A and D315A similar to the *cis* and *trans* constructs used for K308A and D315A experiments. The possible orientation of the subunits in TTCs would be either (a) counterclockwise in top view (K308 in one repeat and K69 in the next repeat form a binding site) or (b) clockwise in top view (K69 in one repeat and K308 in the next repeat form a binding site), as illustrated in Fig. S8 A. For simplicity, the two orientations are shown by triangles of top view, where each

subunit is given in a different color and each corner of the triangle corresponds to one intersubunit ATP-binding site. As we have already shown that the binding of two ATP molecules is sufficient for full activation by voltage- and [ATP]-dependent gating, we examined various configurations of K69A and K308A mutations in
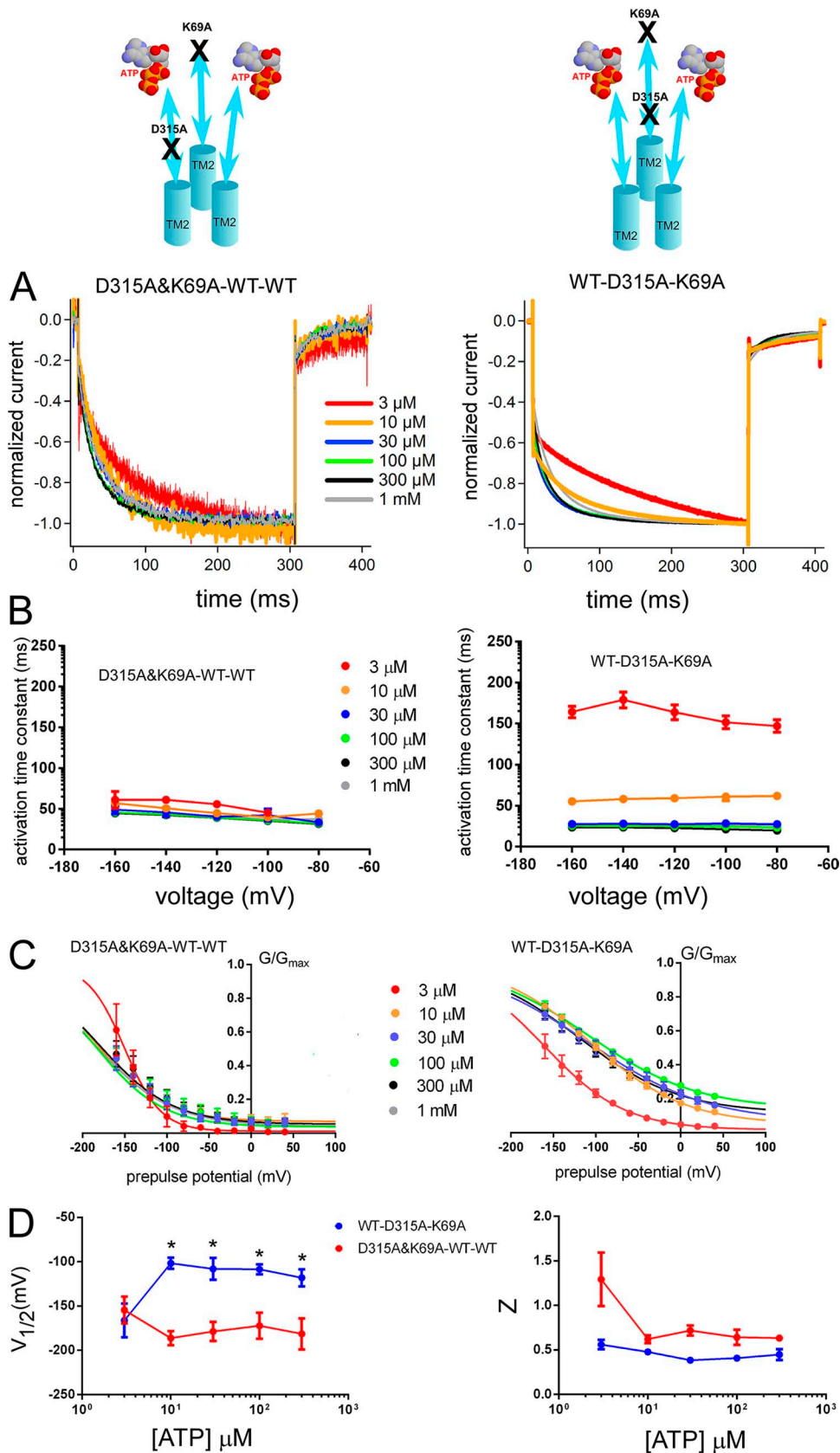
Figure 7. The D315A linker mutation in one subunit shows different voltage- and [ATP]-dependent activation depending on the location relative to one ATP-binding site mutation (K69A) in the tandem trimer molecule. Analysis of D315A&K69A–WT–WT and WT–D315A–K69A shows different voltage- and [ATP]-dependent gating. (A) Normalized Voltage-induced activation traces at −160 mV for D315A&K69A–WT–WT (left) and WT–D315A–K69A (right) at various [ATP] from the representative data shown in Fig. S9. (B) Dependence of the activation time constants on voltage and [ATP] for D315A&K69A–WT–WT (left) and WT–D315A–K69A (right). Mean (± SEM) activation time constants for D315A&K69A–WT–WT (n = 6–10) and WT–D315A–K69A (n = 7–12) at various [ATP] and membrane potentials are shown. (C) Mean (± SEM) normalized G-V relationships at various [ATP] for tandem trimers D315A&K69A–WT–WT (n = 6–10) and WT–D315A–K69A (n = 6–16) derived from the maximum tail current responses at −60 mV by fitting with the two-state Boltzmann equation, as described in Materials and methods from the same oocytes. (D) Mean (± SEM) $V_{1/2}$ (mV) and Z values for the D315A&K69A–WT–WT (n = 6–10) and WT–D315A–K69A (n = 6–16). *, P < 0.05.

the trimer for voltage- and [ATP]-dependent activation. Full activation would indicate that the two mutations are located at the same ATP-binding pocket, and that only one ATP-binding site is disrupted. Therefore, it is possible to determine whether the major trimeric arrangement is counterclockwise (a) or clockwise (b). Our results showed that the counterclockwise orientation (a) is favored, as full activation was observed only for WT–K308A–K69A and K308A–K69A–WT (Fig. S8, B and C).

Next, we prepared TTC constructs that harbor a single K69A and a single D315A mutation, where D315A was located either on an adjacent subunit that receives the ATP-binding signal directly from its own intact ATP-binding site (D315A&K69A–WT–WT) or in direct connection to the mutated ATP-binding site (WT–D315A–K69A). As shown in Fig. S9, both constructs (D315A&K69A–WT–WT and WT–D315A–K69A) showed voltage- and [ATP]-dependent gating. Normalized voltage-induced activation phases in the steady state after the application of [ATP] revealed some important differences (Fig. 7 A). Although D315A&K69A–WT–WT showed a fast voltage-induced activation phase, from −40 to −160 mV, even at low [ATP], in the steady state upon hyperpolarizing step pulses, WT–D315A–K69A showed slow voltage-induced activation at low [ATP] and acceleration in voltage-induced activation kinetics with increasing [ATP] (Fig. 7 A). In Fig. 7 B, activation time constants calculated from single-exponential fittings of the hyperpolarization-induced activation traces at various [ATP] and membrane potentials are shown. Voltage-induced activation time constants at −160 mV for various [ATP] were compared. The results showed that the activation time constants of the two TTCs with different configurations were not similar. Furthermore, the effect of increasing [ATP] on the voltage-induced activation speed of the two configurations was also different (details of the statistical analyses are in the supplemental text).

Analysis of the tail currents at various [ATP] also revealed clear differences for the G-V relationships. As shown in Fig. 7 C, there was no apparent G-V curve shift to depolarized potentials with increasing [ATP] in D315A&K69A–WT–WT. For WT–D315A–K69A, we observed a clear shift of the G-V relationship to depolarized potentials with increasing [ATP]. The results showed that the effect of an increase in [ATP] was different between these two constructs (details of the statistical analyses are in the supplemental text).

In summary, the results showed that D315A&K69A–WT–WT and WT–D315A–K69A were different in terms of both [ATP]-dependent acceleration of voltage-induced activation and G-V curve shifts to depolarized potentials (Fig. 7, B–D). Furthermore, D315A&K69A–WT–WT and WT–D315A–K69A were highly similar to D315A–K308A–WT and WT–D315A&K308A–WT, respectively (Figs. 7 and 6). This similarity suggests that,

rather than the mutation type that disrupts ATP binding, the relative location of D315A with respect to the disrupted ATP-binding site is critical.

Voltage- and [ATP]-dependent gating does not change depending on the location of T339S relative to that of K308A in the trimer with two intact ATP-binding sites

We used a similar *cis* and *trans* comparison approach to evaluate the activation signal transmission from ATP binding to the pore level by using K308A and T339S mutations in the TTC (Figs. S10 and 8). We prepared trimeric constructs with one ATP-binding site disrupted by the K308A mutation and introduced the T339S mutation into the same or adjacent subunits creating *trans* (K308A–T339S–WT) and *cis* (WT–K308A&T339S–WT) configurations. Both constructs showed voltage- and [ATP]-dependent gating (Fig. S10). The results in Fig. 8 showed that the *cis* and *trans* configurations have similar activation time constants, but there was also a slight but statistically significant difference between the effect of the increase in [ATP] on the speed of the voltage-induced activation phase between the two constructs (details of the statistical analyses are in the supplemental text).

We also analyzed different combinations of *trans* constructs WT–K308A–T339S and T339S–WT–K308A to compare with K308A–T339S–WT for any possible position effect. All of the *trans* constructs were similar to each other (not depicted).

In summary, the results showed that the location of a single T339S mutation relative to a single K308A mutation in the TTC did not influence the voltage- and [ATP]-dependent gating remarkably. Furthermore, these results suggest that the activation signal spreads to all subunits at the pore level.

Voltage- and [ATP]-dependent gating does not change depending on the location of a T339S relative to that of D315A

In the previous *cis* and *trans* experiments with two intact ATP-binding sites, we showed that the activation signal from each ATP-binding site is transmitted downward directly on the corresponding β-*14* strand until it reaches the level of D315 (linker region) and spreads to all three subunits at the pore level. We evaluated how the ligand-induced signal travels between the linker and pore levels by preparing *cis* and *trans* constructs of D315A and T339S mutations. We analyzed voltage- and [ATP]-dependent gating of the *trans* (D315A–T339S–WT) and *cis* (WT–D315A&T339S–WT) constructs in the steady state after various [ATP] applications by hyperpolarizing step pulses (Figs. S11 and 9).

Voltage-induced activation time constants at −160 mV for various [ATP] were compared for D315A–T339S–WT and WT–D315A&T339S–WT (Fig. 9, C and D). The results showed that both activation time constants of constructs and the effects of an increase in [ATP] were

highly similar. $V_{1/2}$ (mV) values of D315A–T339S–WT and WT–D315A&T339S–WT at various [ATP] (Fig. 9, E–G) were analyzed. The results showed that the effect of [ATP] increase on $V_{1/2}$ (mV) values of D315A–T339S–WT and WT–D315A&T339S–WT was highly similar (details of the statistical analyses are in the supplemental text).

Z values of D315A–T339S–WT and WT–D315A&T339S–WT at various [ATP] (Fig. 9 H) were analyzed. The results showed that the effect of [ATP] increase on Z values of D315A–T339S–WT and WT–D315A&T339S–WT were highly similar (details of the statistical analyses are in the supplemental text). We also analyzed different combinations of *trans* constructs
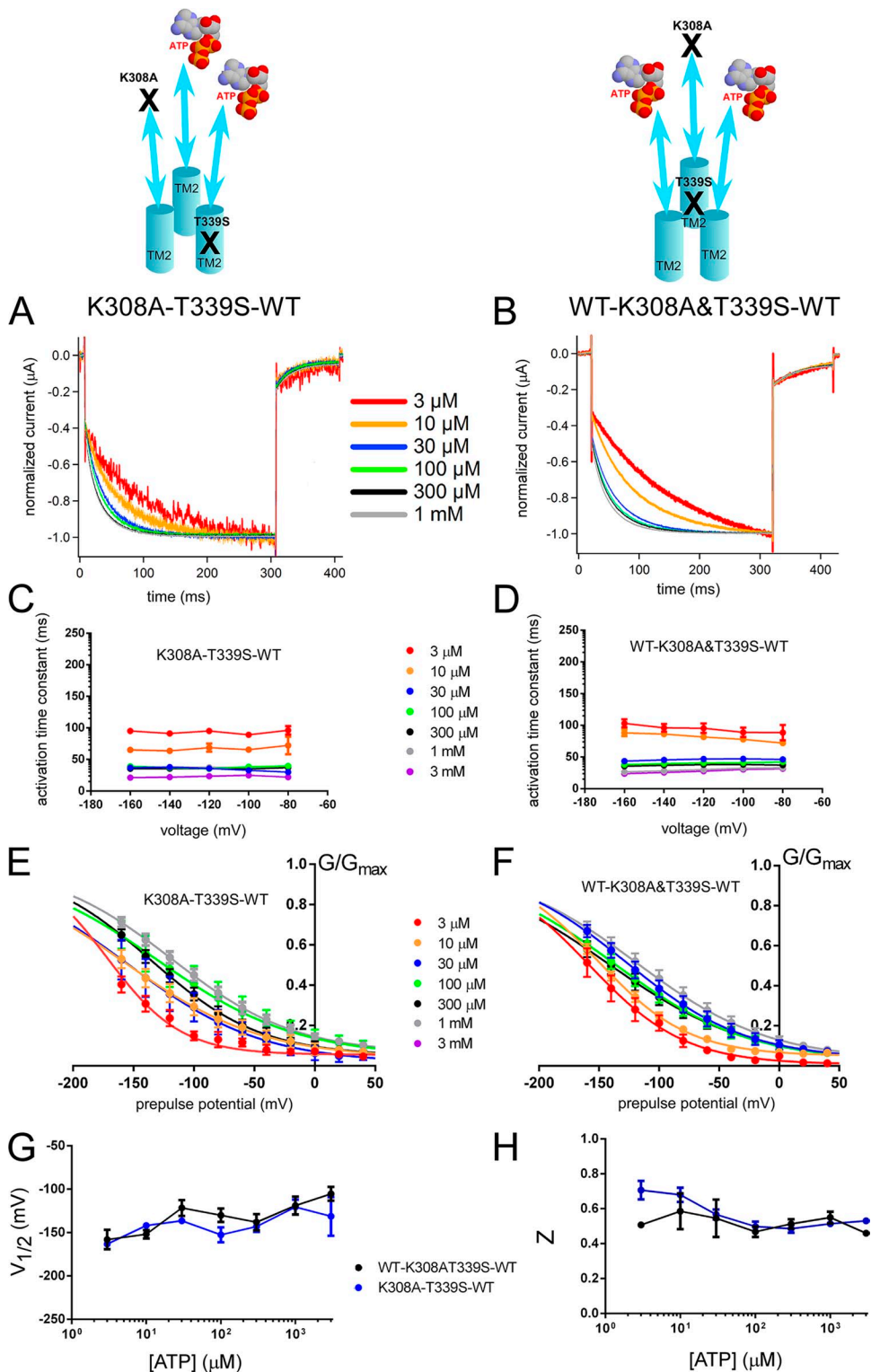
Figure 8. Voltage- and [ATP]-dependent gating does not change depending on the location of one T339S relative to K308A in the trimer with two intact ATP-binding sites; *trans* (K308A–T339S–WT) and *cis* (WT–K308A&T339S–WT) showed similar voltage- and [ATP]-dependent gating. (A and B) Voltage-induced normalized activation traces of *trans* (K308A–T339S–WT; A) and *cis* (WT–K308A&T339S–WT; B) at various [ATP] from the representative traces shown in Fig. S10. (C and D) Dependence of the activation kinetics on voltage and [ATP] for *trans* (C) and *cis* (D) constructs. Mean (± SEM) activation time constants for *trans* (C; n = 5–18) and *cis* (D; n = 6–9) constructs at various [ATP] and membrane potentials are shown. (E and F) Normalized G-V relationships at various [ATP] for *trans* (E) and *cis* (F) constructs derived from the maximum tail current responses by fitting with the two-state Boltzmann equation, as described in Materials and methods. (G and H) Mean (± SEM) $V_{1/2}$ (mV) (G) and Z (H) values for *trans* (C; n = 5–18) and *cis* (D; n = 6–9) constructs.

WT–D315A–T339S and T339S–WT–D315A to compare with those of D315A–T339S–WT for any possible position effect. All of the *trans* constructs were similar to each other (not depicted).

In summary, the results showed that the activation signal spreads to all subunits below the level of the D315 residue in the linker region.

DISCUSSION

The structure of trimeric P2X channels is unique among ligand-gated channels in that each subunit has two TM helices (TM1 and TM2), and its pore is formed by three TM2 helices from each subunit. Because of the inter-subunit configuration of the ATP-binding pocket, each
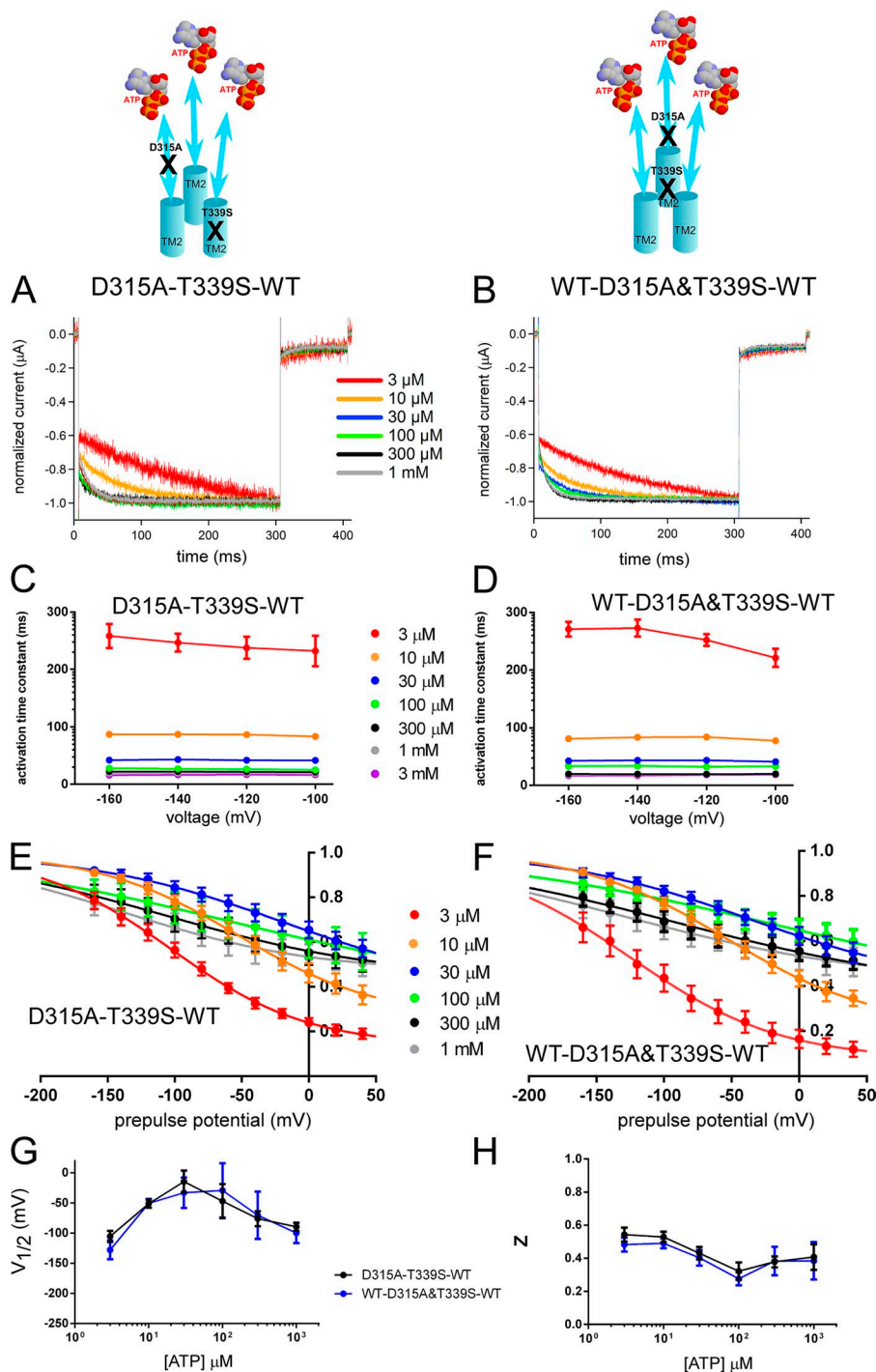
Figure 9. Voltage- and [ATP]-dependent gating does not change depending on the location of one T339S relative to D315A in the trimer; *trans* (D315A–T339S–WT) and *cis* (WT–D315A&T339S–WT) showed similar voltage- and [ATP]-dependent gating. (A and B) Normalized voltage-induced activation traces of *trans* (A) and *cis* constructs (B) at various [ATP] from the representative traces shown in Fig. S11. (C and D) Dependence of the activation kinetics on voltage and [ATP] for *trans* (C) and *cis* constructs. Mean (± SEM) activation time constants for *trans* (C; $n = 12$–16) and *cis* (D; $n = 9$–14) constructs at various [ATP] and membrane potentials are shown. (E and F) Mean (± SEM) normalized G-V relationships at various [ATP] for *trans* (C; $n = 7$–14) and *cis* (D; $n = 6$–10) constructs derived from the maximum tail current responses by fitting with the two-state Boltzmann equation, as described in Materials and methods. (G and H) Mean (± SEM) $V_{1/2}$ (mV) (G) and Z (H) values for the *trans* (C; $n = 7$–14) and *cis* (D; $n = 6$–10) constructs.

ATP-binding site is in direct communication with a TM1 and the pore-forming TM2 via β strands (Fig. 1, D and H). While three TM2 helices are directly involved in the ion permeation pathway, TM1 helices harbor critical residues, which affect the gating indirectly (Jindrichova et al., 2009; Keceli and Kubo, 2009; Li et al., 2010). Previous studies focusing on the structure and function of ligand-gated ion channels (Colquhoun and Sakmann, 1985; Miyazawa et al., 1999, 2003; Grosman and Auerbach, 2000; Unwin et al., 2002; Unwin and Fujiyoshi, 2012) revealed that ligand binding causes allosteric interactions between the subunits that result in several conformational transitions from closed to open (Changeux et al., 1967; Miyazawa et al., 1999). For the $P2X_2$ receptor channel, ligand binding–induced sequential conformational changes also depend on the membrane potential (Fujiwara et al., 2009; Keceli and Kubo, 2009). In this study, we initially evaluated how many bound ATP molecules are necessary and sufficient for both [ATP]- and voltage-induced activation. Thereafter, we attempted to clarify the activation signal transmission route following ATP binding and voltage change.

Implication of the results for the necessary and sufficient number of bound ATP molecules for voltage- and [ATP]-dependent gating

Dose–response relationship analyses of the $P2X_2$ receptor shows that more than one ATP is required to activate the channel, as the Hill coefficient value is close to 2 (Fig. 2, D and E). Previous cysteine-scanning, functional, and structural data revealed the ATP-binding residues as K308, K69, R290, and K71 (Ennion et al., 2000; Jiang et al., 2000; Kawate et al., 2009; Hattori and Gouaux, 2012). In the present study, we used the K308A mutation, which makes the channel unresponsive to even very high concentrations of ATP (>3 mM). This residue is linked to the pore-forming TM2 helix through β-*14* (Fig. 1).

K308 was shown to be involved in gating (Cao et al., 2007; Keceli and Kubo, 2009). For example, the K308A mutation eliminates the spontaneous activity introduced by the T339S mutation at the pore (Cao et al., 2007), whereas the K308R mutation shifts the normalized G-V relationships to more hyperpolarized potentials compared with WT. In our previous study, we successfully simulated the effect of K308R by only changing the k_{off} values of the rate-limiting voltage-dependent step in a three-step two-transition model (Keceli and Kubo, 2009), which suggests that this residue is important for both ATP binding and ATP-induced downstream signal transmission.

By using K308A in the TTCs, we blocked the downstream ligand-induced information transfer from each ATP-binding site at low [ATP] between the 3-µM and 1-mM range. We observed that two intact ATP-binding sites were sufficient and necessary to reproduce the voltage- and [ATP]-dependent gating of the P2X receptor

(Figs. S2 and S3). Our findings are in line with a recent study by Stelmashenko et al. (2012) who analyzed the activation properties of the P2X receptor with one, two, or three K69A mutant subunits and observed that disruption of two ATP-binding sites exclusively abolished activation of the trimer; however, the disruption of only one ATP-binding site did not significantly alter activation kinetics or unitary conductance.

Although the concatemer approach has widely been used in ion channel structure–function studies including those involving P2X (Nagaya et al., 2005; Browne et al., 2011; Heymann et al., 2013), there have been several studies suggesting that this approach does not always guarantee for the correct assembly and stoichiometry of the constructs (McCormack et al., 1992; Hurst et al., 1995; Nicke et al., 2003). For this purpose, we initially confirmed the expression of trimeric constructs by Western blotting (Fig. S1). In the next step, we investigated whether there is any influence of hetero-assembled products, which is the assembly of one subunit of an individual TTC with that of another TTC, as stated in some earlier works (McCormack et al., 1992; Hurst et al., 1995; Stoop et al., 1999). For this purpose, we prepared a set of TTCs harboring two WT and one subunit harboring two ATP-binding site mutants K308A and K69A (K308A&K69A–WT–WT, WT–K308A&K69A–WT, and WT–WT–K308A&K69A). These three test constructs are expected to be nonfunctional, as two ATP-binding sites on the left end and the right end of the mutant subunits, which will eventually lead to the disturbance of two ATP-binding sites in the trimer and any activation by not too high [ATP], would indicate the presence of cross-assembly products of the WT subunits from different trimers. We monitored the activation levels of these new constructs by daily recordings from the same oocytes after injection of similar concentrations of RNA (50 nl of 5 ng/µl). In days 1 and 2 after RNA injection (which is the time interval for our experimental protocols to avoid high expression levels), the new constructs did not show any prominent activation in response to 1 mM [ATP] (Fig. S12). From the third day and later on, we observed activation of the constructs, indicating that cross-assembly occurs at only high expression levels, which is not the case for our experimental conditions. There remains a possibility that the lack of hetero assembly of these three test constructs is caused by the exceptionally low expression compared with other constructs. Thus, we examined the expression level of the three test constructs and confirmed that their expression level is not lower, and in fact is even higher, than other constructs (Fig. S13).

Further supporting evidence that the TTCs are functioning as the planned trimeric tandems rather than creating hetero-assembled products arises from the detailed analyses of their voltage- and [ATP]-dependent gating. One important piece of evidence is the similar

phenotypes of K308A–D315A–WT and D315A&K69A–WT–WT. The similarity of the gating of these two constructs strongly suggests that the contribution of the hetero-assembly among tandem trimers is negligible. Moreover, the experiments to reveal the subunit order (Fig. S8) showed clear differences between K69A–K308A–WT and K308A–K69A–WT (also WT–K308A–K69A), again showing that a possibility of cross-assembly is not likely. In summary, evidence strongly supports that the channels are functioning as planned tandem trimers in our experiments, and that the influence of cross-assembly is negligible, if there is any, in low expression levels.

The overall results suggest that with only two ATP molecules bound, the native voltage- and [ATP]-dependent gating properties, such as [ATP]-dependent acceleration of the voltage-induced activation phase and the G-V curve shift to depolarized potentials, are conserved (Fig. 2, A and C). The results reveal that normal gating of the trimeric receptor requires at least two intact ATP-binding sites.

Implication of the results for D315A and T339S in the linker and pore

In the next step, we evaluated the activation signal transmission upon ATP binding and voltage change. For this purpose, we used the critical mutations D315A and T339S that reside at certain levels between the ATP-binding and pore regions (Fig. 1), and radically change the gating properties of the channel.

The D315A mutation in the β-*14* linker between the ATP-binding site and TM2 creates two different gating modes with a double-shoulder dose–response relationship (Figs. 3, A and B, and S5). This unique gating property observed with D315A might be caused by a disruption of the β-strand structure that results in a decrease of the energy barrier that holds the channel in the closed state. It is unlikely that the D315A effect comes from an electrostatic interaction, as the D315K mutation was similar to WT (not depicted). The D315 residue in the linker domain is conserved in all P2X family members, suggesting its critical role in channel activation.

When we introduced the D315A mutation into two or three subunits, the main D315A effect, an emergence of two different gating modes, was prominent. However, when we introduced the D315A mutation into only one subunit, the phenotype was similar to that of WT (Figs. 4 and S6). The effect of the number of subunits harboring the D315A mutation was similar to that observed with the K308A mutation. This finding further supports that two intact subunits are necessary for the full transmission of the activation signal to the pore.

The T339 residue is located at the narrowest part of the pore of the P2X$_2$ receptor channel (Kawate et al., 2009; Li et al., 2010; Hattori and Gouaux, 2012; Fig. 1, C and G). This residue is critical for the gating of P2X$_2$

(Keceli and Kubo, 2009). The T339S mutation facilitates voltage- and [ATP]-dependent gating and makes the channel voltage independent at saturating concentrations of ATP (Keceli and Kubo, 2009). As the T339S mutation in the pore significantly changed the voltage sensitivity of the channel, we used this mutation effect to analyze the contribution of individual subunits to pore opening in voltage- and [ATP]-dependent gating. The effect of the T339S mutation was different when inserted into one, two, or three subunits in the tandem trimeric structure. When all three subunits harbored T339S, voltage-dependent gating was abolished at saturating concentrations of ATP (Fig. 5 A). When we swapped the T339S mutant subunits with WT subunits in the trimer one by one, we observed a gradual rescue of the voltage- and [ATP]-dependent gating at saturating concentrations of ATP (Fig. 5, B–E).

Single-channel analysis of the T339K mutation revealed a gradual increase in the chloride permeability and a decrease in unitary conductance with increasing number of T339K mutations in the trimer, and it was suggested that pore opening is symmetric in the P2X$_2$ trimer (Browne et al., 2011). In our study, the gradual changes in voltage-dependent gating parameters upon the insertion of T339S mutations in the trimer suggest that the transition of the channel from closed to open requires incremental contribution of subunits to the final pore opening, which in turn, requires equal and possibly symmetric spread of the activation signal from the upper domains.

Markov models show that single-exponential voltage-induced activation of voltage- and [ATP]-dependent gating requires the binding of two ATP molecules for pore opening

It is critical that the results observed for pore level mutations in the tandem repeat constructs were different from that of linker and ATP-binding region mutations. While two intact subunits are necessary for the transmission of the ATP-binding and voltage change signals to the pore, pore opening requires equal and gradual contribution of all subunits. This raises a fundamental question of how the activation signal is transmitted symmetrically to the pore level.

We prepared three different Markov models to gain insight into how seemingly contradictory findings of the sufficiency of two intact ATP-binding sites and linker for activation and the equal contribution of subunits on the final pore opening can converge. We used the fast ATP-binding and the rate-limiting voltage-dependent rate constants that were derived from the macroscopic rate constants for individual subunits' transition rates (Fujiwara et al., 2009; Keceli and Kubo, 2009) and analyzed the voltage-induced activation phases (Fig. 10), as described in detail in Materials and methods. We focused on the voltage-induced activation phase in the

steady state at various [ATP] and assumed that the ATP-binding rate of each subunit is constant. The simulation results showed that the activation phase at the lowest experimental concentration (3 µM ATP) could not be fitted by a single-exponential function in the first model, where the channel activation was firmly dependent on three ATP molecules binding (Fig. 10 A). However, in the models where the binding of two ATP molecules was sufficient to open the channel, the simulation data could be successfully fitted by a single-exponential function just like our experimental data (Fig. 10, B and C).

It is important to mention that, in very low [ATP] (e.g., 0.3 µM), it is possible to see deviations from a single-exponential activation phase to sigmoidicity, even for the models where the binding of two ATP molecules is sufficient for opening the channel. Therefore, we examined

A

$C\ C\ C \xrightleftharpoons[k_{unbind}]{3x\ k_{bind}\ x\ [ATP]} CA\ C\ C \xrightleftharpoons[2x\ k_{unbind}]{2x\ k_{bind}\ x\ [ATP]} CA\ CA\ C \xrightleftharpoons[3x\ k_{unbind}]{k_{bind}\ x\ [ATP]} CA\ CA\ CA$

$k_{on} \rightleftharpoons k_{off}$ $2xk_{on} \rightleftharpoons k_{off}$ $3xk_{on} \rightleftharpoons k_{off}$

$OA\ C\ C \xrightleftharpoons[k_{unbind}]{k_{bind}\ x\ [ATP]} OA\ CA\ C \xrightleftharpoons[2x\ k_{unbind}]{k_{bind}\ x\ [ATP]} OA\ CA\ CA$

$k_{on} \rightleftharpoons 2xk_{off}$ $2xk_{on} \rightleftharpoons 2xk_{off}$

$OA\ OA\ C \xrightleftharpoons[k_{unbind}]{k_{bind}\ x\ [ATP]} OA\ OA\ CA$

$k_{on} \rightleftharpoons 3xk_{off}$

$OA\ OA\ OA$

$C \xrightleftharpoons[k_{unbind}]{k_{bind}\ x\ [ATP]} CA \xrightleftharpoons[k_{off}]{k_{on}} OA$

A (3,3)

3 ATP can bind
all 3 ATP binding
can only open the pore

B

B (3,2)

3 ATP can bind
2 ATP binding
can open
the pore

C

C (2,2)

Only 2 ATP can bind
2 ATP binding opens the pore

(Graphs: normalized current vs time (ms), 0–300. Traces for 3 µM (red), 10 µM (orange), 30 µM (blue), 100 µM (green), 300 µM (black), with dashed black single-exponential fittings.)

Figure 10. Evaluation of how the binding of two ATP molecules for channel activation and the independent contribution of three subunits to the final pore opening can converge using Markov models. The voltage-induced activation phase of the simulation was compared with experimental data for the lowest activating [ATP]. State diagrams for different Markov models (A–C), which were based on the assumption that each subunit is independent and passes through two transitions, $C \rightleftharpoons CA \rightleftharpoons OA$, with a fast ATP-binding and a rate-limiting voltage-dependent step. (Details of the model are given in Materials and methods.) (A) 10-step model with three intact ATP-binding sites, which requires the binding of three ATP molecules for full activation. (B) 10-step model with three intact ATP-binding sites that can be activated by the binding of two ATP molecules. (C) Six-step model with only two intact ATP-binding sites, which can be activated by the binding of two ATP molecules. Next to each model diagram, simulation traces for voltage-induced activation at various [ATP] are shown (traces for 3, 10, 30, 100, and 300 µM ATP are shaded in red, orange, blue, green, and black, respectively). Dashed black lines show single-exponential fittings of the voltage-induced activation phase at 3 µM ATP. Note the apparent sigmoidicity of voltage-induced activation for model A, which could not be fitted by a single-exponential function (shown by the arrow). Simulation traces of the models in B and C were almost successfully fitted by a single-exponential function.

the models at 3 µM ATP, which is the lowest ATP concentration at which the macroscopic activation of the channel can be observed by voltage-induced step pulses in steady-state activation.

The models show that when the trimer can be firmly activated by the binding of two ATP molecules, independent transitions of the subunits can simulate the single-exponential activation phase. This result suggests that the contributions of the subunits to the final pore opening of the trimer can be symmetric and independent because of the equal distribution of the activation signal at the pore level.

Implication of the results of *cis* and *trans* mutations in the TTC for the activation signal transmission from ATP binding to the pore

To obtain an insight into the activation signal transmission from ATP binding to gate, we prepared TTCs that harbor one D315A or T339S mutation below one K308A mutation that eliminates the ATP binding.

We first evaluated the *cis* and *trans* configurations of D315A and K308A mutations. In the *cis* configuration, these mutations are aligned on the same structural path (β-*14* strand); therefore, this construct probes the signal transmission over a single subunit from one ATP-binding site to the level of the D315 residue. In the *trans* configuration, the D315A mutation subunit has an intact ATP-binding site, and the K308A mutation disrupts ATP binding in an adjacent subunit. Comparison of the effects of *cis* and *trans* configurations would show how the activation signal from each ATP-binding site projects downward through the linker domains.

We observed that voltage- and [ATP]-dependent gating of *cis* (WT–D315A&K308A–WT) and *trans* (K308A–D315A–WT) configurations were strikingly different in terms of both [ATP]-dependent acceleration of voltage-induced activation traces and G-V curve shifts (Figs. 6 and S7). The results suggest that the activation signal for each ATP-binding site is directly projected downward through its corresponding β strand to the level of D315.

Next, we analyzed the activation signal transmission from the ATP-binding site to the pore. We prepared *cis* and *trans* TTCs that harbor two mutations, K308A in the ATP-binding region and T339S at the pore level, which were located at the same (*cis*, WT–K308A&T339S–WT) or adjacent (*trans*, K308A–T339S–WT) subunits and analyzed for voltage- and [ATP]-dependent gating (Figs. 8 and S10). Contrary to the results obtained from K308A–D315A *cis/trans* experiments, we did not observe remarkable differences with respect to the position of the single T339S mutant relative to the ATP-binding site mutation. The results suggest that the final pore opening of the trimer receives the activation signal from all three subunits.

As the last step, we prepared *cis/trans* constructs that harbor the D315A mutation at the linker and the T339S

mutation at the pore, on the same or adjacent subunits. When we compared the *trans* (D315A–T339S–WT) and *cis* (WT–D315A&T339S–WT) constructs for voltage- and [ATP]-dependent gating, we did not observe remarkable differences (Figs. 9 and S11). This finding further supports our interpretation that the final pore opening of the P2X$_2$ receptor receives the activation signal from all three subunits.

The overall *cis/trans* experiment results suggest that the activation signal from each ATP-binding site projects directly through the linker domains down to the level of D315, whereas the activation signal spreads to all three subunits at the pore level as illustrated in Fig. 11.

Implication of the results for the crystal structure data and subunit cooperativity

The comparison of the closed- and open-state structures of P2X receptors (Kawate et al., 2009; Hattori and Gouaux, 2012) revealed differences in the extracellular domains and pore-forming TM helices. In the open-state structure, there is bending of the β sheets linking
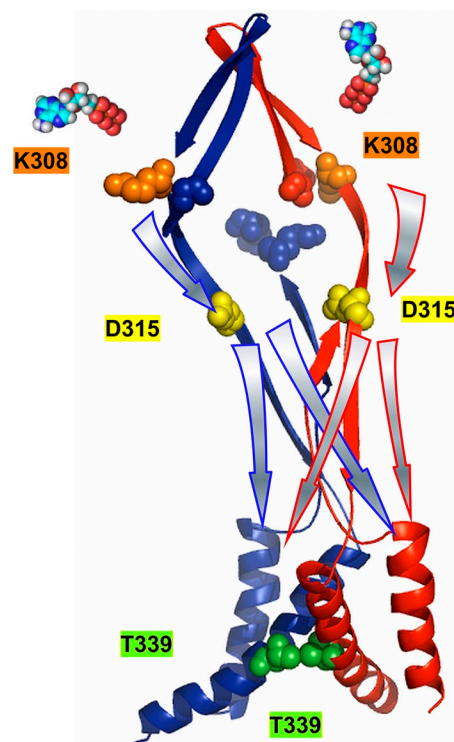
Figure 11. Schematic presentation of the activation signal transmission from two ATP-binding sites to the pore upon voltage- and [ATP]-dependent activation. For simplicity, two subunits are illustrated in red and blue. Colored spheres mark the K308 (orange) and K69 (blue) residues in the ATP-binding region, D315 (yellow) in the linker, and T339 (green) at the pore level. Arrows with the same color of borderlines with the subunits depict the signal transmission on each subunit. The activation signal from one intersubunit ATP binding flows directly on the corresponding β-*14* strand of the ATP-binding site down to the D315 level, and then spreads to other subunits at the pore level.

the ATP-binding site to the TM helices, suggesting a prominent role for the β strands in activation signal transmission. Based on the comparison of snapshot views of the closed and open channel, bending of the β-sheet structures is likely to precede the expansion of TM helices and pore opening. The β-sheet structures' functional importance in the transmission of ligand signal to pore domains has also been reported in cys-loop receptors (Venkatachalan and Czajkowski, 2012). The unique effect of the D315A mutation in our study is likely to be caused by its structural localization on the β-*14* strand that is directly linked to the pore-forming TM2.

Another prominent difference observed between the two structures is that, compared with the closed state, subunit–subunit interactions weaken, especially for the TM domains in the open state (Fig. 1). This structural feature suggests that by ligand binding, the trimer rearranges itself from a closed compact structure to an open state in which the subunit interactions start to loosen with large intersubunit crevices. However, it is still difficult to predict the role of subunit–subunit interactions from the snapshot views or models of the closed and open structures without knowing the transitional states in between. In our study, we introduced the mutations in a hierarchy from the ligand-binding site to the pore; therefore, our functional data provide clues as to the cooperativity and individual contribution of each subunit at different levels from ligand-binding site to pore.

It is possible to analyze the subunit interactions in gating from a functional point of view by inserting mutations, which change the gating drastically in a subunit-specific manner (Horovitz and Fersht, 1990; Zandany et al., 2008). Using the thermodynamic double mutant cycle analysis method (Zandany et al., 2008), we were able to calculate the magnitude of intersubunit coupling free energy between subunit pairs for the mutations at the pore (T339S) and linker (D315A) levels. With this approach, we can at least have an insight into the possible subunit–subunit interaction differences at the linker and pore levels, which might improve the interpretation of results of the *cis*/*trans* experiments.

In the thermodynamic double mutant cycle analysis, the equilibrium effect of each mutation on function is evaluated stepwise. Free energy differences (ΔG) of one, two, and three subunit mutations from WT, single, and two subunit mutations would give Δ*G1*, Δ*G2*, and Δ*G3*, respectively. If the subunits operate independently, the conformational changes of the adjacent subunits would not affect each other and therefore, the stepwise increase in the number of mutations in the trimer would result in similar free energy differences for each step. On the other hand, when free energy differences are not equal, adjacent subunits could be considered as coupled. We calculated the free energy differences between the closed and open states of WT–WT–WT, single, double, and triple mutants for T339S and D315A

from the G-V relationships shown in Figs. 4 and 5, using the equation $\Delta G = -RT \ln [O/C]$ at saturating concentrations of ATP at 0 mV (Fig. S14).

The introduction of each T339S mutation at the pore level created similar changes in ΔG values that can be fitted successfully with a linear regression line with a constant slope (Fig. S14 A). However, for D315A mutations at the linker level, ΔG values versus the number of mutations did not show a linear relationship (Fig. S14 B). These results suggest different levels of subunit–subunit interactions at linker and pore levels, which might have caused the functional outcomes of the *cis* and *trans* mutations that were distinct for linker and pore levels.

A strong coupling of subunits at ATP-binding sites has been reported previously. Based on maximum likelihood fittings of the single-channel data, Ding and Sachs (1999) concluded that ATP-binding/unbinding rates differ through the sequential bindings of ATP to the trimer, indicating that ATP-binding sites are not independent and that ATP binding to one site modifies the other in a positive cooperative manner. Recently, the Swartz group proposed a novel membrane-embedded P2X4z open-state structure model (Heymann et al., 2013), which is slightly different from the detergent-solubilized open-state crystal structure (Hattori and Gouaux, 2012). This novel open-state model suggests that instead of large intersubunit crevices, there exist intersubunit interactions within the TM domains, which are created by small rotations, and translation of the TM2 helix toward the central axis. Moreover, the intersubunit interactions at the TM helices appear to be at rather deeper localizations at the lower ends of TM domains. In line with our pore mutation (T339S) data, which suggest independent contribution of subunits to gating and spread of activation signal at the pore level, it is possible that as the channel rearranges from closed to open, the intersubunit interactions loosen gradually, and at the final pore opening, subunits become relatively more independent with limited interactions at the lower ends of TM domains. The difference in subunit stoichiometry from ligand binding to gating for the nicotinic acetylcholine receptor has also been shown by Unwin and Fujiyoshi (2012), using the plunge-freezing technique. Their results showed that after ligand binding, symmetric outward displacement of the extracellular domains propagates to the pore, disrupts the symmetry, and leads to an asymmetric pore opening. Asymmetric appearance of the pore opening was suggested to be the result of the unstable assembly of the M2 helices in the closed state (Unwin and Fujiyoshi, 2012).

Our results suggest that the ATP-binding signal projects downward directly on the corresponding β-*14* strand, and then spreads equally to all three subunits, as illustrated in Fig. 11. The functional data we obtained in this study gives insight into how ligand binding–induced allosteric transitions among individual subunits are projected

to the active site of the receptor channel, which is located at a considerable distance from the ligand-binding site.

REFERENCES

Arnold, K., L. Bordoli, J. Kopp, and T. Schwede. 2006. The SWISS-MODEL workspace: a web-based environment for protein structure homology modelling. *Bioinformatics.* 22:195–201. http://dx.doi.org/10.1093/bioinformatics/bti770

Bordoli, L., F. Kiefer, K. Arnold, P. Benkert, J. Battey, and T. Schwede. 2009. Protein structure homology modeling using SWISS-MODEL workspace. *Nat. Protoc.* 4:1–13. http://dx.doi.org/10.1038/nprot.2008.197

Brake, A.J., M.J. Wagenbach, and D. Julius. 1994. New structural motif for ligand-gated ion channels defined by an ionotropic ATP receptor. *Nature.* 371:519–523. http://dx.doi.org/10.1038/371519a0

Browne, L.E., L.S. Cao, H.E. Broomhead, L. Bragg, W.J. Wilkinson, and R.A. North. 2011. P2X receptor channels show threefold symmetry in ionic charge selectivity and unitary conductance. *Nat. Neurosci.* 14:17–18. http://dx.doi.org/10.1038/nn.2705

Burnstock, G. 2007a. Physiology and pathophysiology of purinergic neurotransmission. *Physiol. Rev.* 87:659–797. http://dx.doi.org/10.1152/physrev.00043.2006

Burnstock, G. 2007b. Purine and pyrimidine receptors. *Cell. Mol. Life Sci.* 64:1471–1483. http://dx.doi.org/10.1007/s00018-007-6497-0

Burnstock, G. 2008. Non-synaptic transmission at autonomic neuroeffector junctions. *Neurochem. Int.* 52:14–25. http://dx.doi.org/10.1016/j.neuint.2007.03.007

Cao, L., M.T. Young, H.E. Broomhead, S.J. Fountain, and R.A. North. 2007. Thr339-to-serine substitution in rat P2X2 receptor second transmembrane domain causes constitutive opening and indicates a gating role for Lys308. *J. Neurosci.* 27:12916–12923. http://dx.doi.org/10.1523/JNEUROSCI.4036-07.2007

Changeux, J.P., J. Thiéry, Y. Tung, and C. Kittel. 1967. On the cooperativity of biological membranes. *Proc. Natl. Acad. Sci. USA.* 57:335–341. http://dx.doi.org/10.1073/pnas.57.2.335

Colquhoun, D., and A.G. Hawkes. 2009. A Q-matrix cookbook. How to write only one program to calculate the single-channel and macroscopic predictions for any kinetic mechanisms. *In* Single-Channel Recording. B. Sakmann and E. Neher, editors. Springer, New York. 589–636.

Colquhoun, D., and B. Sakmann. 1985. Fast events in single-channel currents activated by acetylcholine and its analogues at the frog muscle end-plate. *J. Physiol.* 369:501–557.

Ding, S., and F. Sachs. 1999. Single channel properties of P2X$_2$ purinoceptors. *J. Gen. Physiol.* 113:695–720. http://dx.doi.org/10.1085/jgp.113.5.695

Ennion, S., S. Hagan, and R.J. Evans. 2000. The role of positively charged amino acids in ATP recognition by human P2X1 receptors. *J. Biol. Chem.* 275:35656. http://dx.doi.org/10.1074/jbc.M003637200

Fujiwara, Y., and Y. Kubo. 2004. Density-dependent changes of the pore properties of the P2X2 receptor channel. *J. Physiol.* 558:31–43. http://dx.doi.org/10.1113/jphysiol.2004.064568

Fujiwara, Y., B. Keceli, K. Nakajo, and Y. Kubo. 2009. Voltage- and [ATP]-dependent gating of the P2X$_2$ ATP receptor channel. *J. Gen. Physiol.* 133:93–109. http://dx.doi.org/10.1085/jgp.200810002

Grosman, C., and A. Auerbach. 2000. Kinetic, mechanistic, and structural aspects of unliganded gating of acetylcholine receptor channels: A single-channel study of second transmembrane segment 12′ mutants. *J. Gen. Physiol.* 115:621–635. http://dx.doi.org/10.1085/jgp.115.5.621

Hattori, M., and E. Gouaux. 2012. Molecular mechanism of ATP binding and ion channel activation in P2X receptors. *Nature.* 485:207–212. http://dx.doi.org/10.1038/nature11010

Hawkes, A.G., and A.M. Sykes. 1990. Equilibrium distributions of finite-state Markov processes. *IEEE Trans. Reliab.* 39:592–595. http://dx.doi.org/10.1109/24.61316

Heymann, G., J. Dai, M. Li, S.D. Silberberg, H.X. Zhou, and K.J. Swartz. 2013. Inter- and intrasubunit interactions between transmembrane helices in the open state of P2X receptor channels. *Proc. Natl. Acad. Sci. USA.* 110:E4045–E4054. http://dx.doi.org/10.1073/pnas.1311071110

Horovitz, A., and A.R. Fersht. 1990. Strategy for analysing the cooperativity of intramolecular interactions in peptides and proteins. *J. Mol. Biol.* 214:613–617. http://dx.doi.org/10.1016/0022-2836(90)90275-Q

Hurst, R.S., R.A. North, and J.P. Adelman. 1995. Potassium channel assembly from concatenated subunits: effects of proline substitutions in S4 segments. *Receptors Channels.* 3:263–272.

Inoue, K., M. Tsuda, and S. Koizumi. 2005. ATP receptors in pain sensation: Involvement of spinal microglia and P2X(4) receptors. *Purinergic Signal.* 1:95–100. http://dx.doi.org/10.1007/s11302-005-6210-4

Jiang, L.H., F. Rassendren, A. Surprenant, and R.A. North. 2000. Identification of amino acid residues contributing to the ATP-binding site of a purinergic P2X receptor. *J. Biol. Chem.* 275:34190–34196. http://dx.doi.org/10.1074/jbc.M005481200

Jindrichova, M., V. Vavra, T. Obsil, S.S. Stojilkovic, and H. Zemkova. 2009. Functional relevance of aromatic residues in the first transmembrane domain of P2X receptors. *J. Neurochem.* 109:923–934. http://dx.doi.org/10.1111/j.1471-4159.2009.06021.x

Kawate, T., J.C. Michel, W.T. Birdsong, and E. Gouaux. 2009. Crystal structure of the ATP-gated P2X$_4$ ion channel in the closed state. *Nature.* 460:592–598. http://dx.doi.org/10.1038/nature08198

Keceli, B., and Y. Kubo. 2009. Functional and structural identification of amino acid residues of the P2X2 receptor channel critical for the voltage- and [ATP]-dependent gating. *J. Physiol.* 587:5801–5818. http://dx.doi.org/10.1113/jphysiol.2009.182824

Khakh, B.S. 2001. Molecular physiology of P2X receptors and ATP signalling at synapses. *Nat. Rev. Neurosci.* 2:165–174. http://dx.doi.org/10.1038/35058521

Khakh, B.S., G. Burnstock, C. Kennedy, B.F. King, R.A. North, P. Séguéla, M. Voigt, and P.P. Humphrey. 2001. International union of pharmacology. XXIV. Current status of the nomenclature and properties of P2X receptors and their subunits. *Pharmacol. Rev.* 53:107–118.

Kiefer, F., K. Arnold, M. Künzli, L. Bordoli, and T. Schwede. 2009. The SWISS-MODEL Repository and associated resources. *Nucleic*

Acids Res. 37:D387–D392. http://dx.doi.org/10.1093/nar/gkn750

Kubo, Y., Y. Fujiwara, B. Keceli, and K. Nakajo. 2009. Dynamic aspects of functional regulation of the ATP receptor channel P2X2. *J. Physiol.* 587:5317–5324. http://dx.doi.org/10.1113/jphysiol.2009.179309

Li, M., T. Kawate, S.D. Silberberg, and K.J. Swartz. 2010. Pore-opening mechanism in trimeric P2X receptor channels. *Nat Commun.* 1:1–7 http://dx.doi.org/10.1038/ncomms1048

McCormack, K., L. Lin, L.E. Iverson, M.A. Tanouye, and F.J. Sigworth. 1992. Tandem linkage of Shaker K⁺ channel subunits does not ensure the stoichiometry of expressed channels. *Biophys. J.* 63:1406–1411. http://dx.doi.org/10.1016/S0006-3495(92)81703-4

Miyazawa, A., Y. Fujiyoshi, M. Stowell, and N. Unwin. 1999. Nicotinic acetylcholine receptor at 4.6 Å resolution: transverse tunnels in the channel wall. *J. Mol. Biol.* 288:765–786. http://dx.doi.org/10.1006/jmbi.1999.2721

Miyazawa, A., Y. Fujiyoshi, and N. Unwin. 2003. Structure and gating mechanism of the acetylcholine receptor pore. *Nature.* 423:949–955. http://dx.doi.org/10.1038/nature01748

Nagaya, N., R.K. Tittle, N. Saar, S.S. Dellal, and R.I. Hume. 2005. An intersubunit zinc binding site in rat P2X2 receptors. *J. Biol. Chem.* 280:25982–25993. http://dx.doi.org/10.1074/jbc.M504545200

Nicke, A., J. Rettinger, and G. Schmalzing. 2003. Monomeric and dimeric byproducts are the principal functional elements of higher order P2X1 concatamers. *Mol. Pharmacol.* 63:243–252. http://dx.doi.org/10.1124/mol.63.1.243

North, R.A. 2002. Molecular physiology of P2X receptors. *Physiol. Rev.* 82:1013–1067.

Nour-Eldin, H.H., F. Geu-Flores, and B.A. Halkier. 2010. USER cloning and USER fusion: The ideal cloning techniques for small and big laboratories. *Methods Mol. Biol.* 643:185–200. http://dx.doi.org/10.1007/978-1-60761-723-5_13

Stelmashenko, O., U. Lalo, Y. Yang, L. Bragg, R.A. North, and V. Compan. 2012. Activation of trimeric P2X2 receptors by fewer than three ATP molecules. *Mol. Pharmacol.* 82:760–766. http://dx.doi.org/10.1124/mol.112.080903

Stoop, R., S. Thomas, F. Rassendren, E. Kawashima, G. Buell, A. Surprenant, and R.A. North. 1999. Contribution of individual subunits to the multimeric P2X₂ receptor: Estimates based on methanethiosulfonate block at T336C. *Mol. Pharmacol.* 56:973–981.

Unwin, N., and Y. Fujiyoshi. 2012. Gating movement of acetylcholine receptor caught by plunge-freezing. *J. Mol. Biol.* 422:617–634. http://dx.doi.org/10.1016/j.jmb.2012.07.010

Unwin, N., A. Miyazawa, J. Li, and Y. Fujiyoshi. 2002. Activation of the nicotinic acetylcholine receptor involves a switch in conformation of the α subunits. *J. Mol. Biol.* 319:1165–1176. http://dx.doi.org/10.1016/S0022-2836(02)00381-9

Valera, S., N. Hussy, R.J. Evans, N. Adami, R.A. North, A. Surprenant, and G. Buell. 1994. A new class of ligand-gated ion channel defined by P2x receptor for extracellular ATP. *Nature.* 371:516–519. http://dx.doi.org/10.1038/371516a0

Venkatachalan, S.P., and C. Czajkowski. 2012. Structural link between γ-aminobutyric acid type A (GABAA) receptor agonist binding site and inner β-sheet governs channel activation and allosteric drug modulation. *J. Biol. Chem.* 287:6714–6724. http://dx.doi.org/10.1074/jbc.M111.316836

Zandany, N., M. Ovadia, I. Orr, and O. Yifrach. 2008. Direct analysis of cooperativity in multisubunit allosteric proteins. *Proc. Natl. Acad. Sci. USA.* 105:11697–11702. http://dx.doi.org/10.1073/pnas.0804104105

Zhou, Z., and R.I. Hume. 1998. Two mechanisms for inward rectification of current flow through the purinoceptor P2X2 class of ATP-gated channels. *J. Physiol.* 507:353–364. http://dx.doi.org/10.1111/j.1469-7793.1998.353bt.x